UNIVERSITY OF OKLAHOMA

GRADUATE COLLEGE

IMPROVED VERTICAL COUPLING BETWEEN PRINTED PLANAR TRANSMISSION LINES

A THESIS

SUBMITTED TO THE GRADUATE FACULTY

in partial fulfillment of the requirements for the

Degree of

MASTER OF SCIENCE

By

AIMEE MATLAND
Norman, Oklahoma
2016

IMPROVED VERTICAL COUPLING BETWEEN PRINTED PLANAR TRANSMISSION LINES

A THESIS APPROVED FOR THE
SCHOOL OF ELECTRICAL AND COMPUTER ENGINEERING

BY

Dr. Jessica Ruyle, Chair

Dr. Tyrone Roach

Dr. Hjalti Sigmarsson

Table of Contents

List of Figures

Abstract

In microwave devices, an aperture is often used as a radiating antenna element or to direct energy vertically from a feed line on one layer of a circuit to another. Researchers have employed many methods to describe the power transfer between a microstrip feed and a finite slot with little agreement between models. Many of these models are backed with rigorous theory that approach the computational complexity of a full wave solver like the High Frequency Structure Simulator (HFSS) which relies on the computationally intensive finite element method. This thesis proposes a novel approach to analytically model the coupling between a microstrip line feeding a finite slot in a ground plane. It attempts to alleviate the computational intensity of some previous methods of describing coupling between a microstrip and a slot while employing a more rigorous analysis than other simple closed-form analysis approaches. This research analyzes the concept of field reciprocity which has been a common theoretical backing for many existing theories as well as stored energy coupling relations. Beyond this, an equivalent circuit model is developed to describe the coupling at the transition region existing primarily inside the dielectric between a slot aperture in a ground plane and a microstrip feed line. Ultimately, this research provides a fundamental theoretical framework for models of vertical coupling between microstrip lines and finite apertures as well as other types of printed planar feed lines such as strip lines and slot lines.

Chapter 1

Introduction

Feeding a radiating slot antenna with a microstrip line reduces fabrication complexity with printed circuit board (PCB) fabrication techniques. Figures 1.1 and 1.2 show two variations of radiating slots that are fed with coaxial lines. These feed structures for the slots employ baluns because a coaxial cable is an unbalanced line [8]. A dyson balun like the one shown in Figure 1.1 adds a physical size requirement that limits a designer from achieving a miniaturized design when they choose to use a coaxial cable as the feed line [9]. Beyond this, time must be taken to curve the center pin of the coaxial line across the slot antenna width where it is then soldered. The dyson balun is also soldered along the ground plane. Figures 1.1, 1.2, and 1.3 serve to represent some of the benefits of feeding a structure with a microstrip line. Figure 1.3(a) shows a microstrip line with a fan-like stub. This microstrip line, a balanced type of transmission line, is printed on the opposite side of the end-loaded slot shown in Figure 1.3(b). With the use of a microstrip feed line such as this, the feedline is no longer restricted in size as it is when using a dyson-type of balun like in Figures 1.1 and 1.2 which may be up to a half wavelength long to operate correctly [1]. During mass-production using PCB fabrication techniques, this type of feed is much faster to produce because it takes out a conductor-merging or soldering step since the feed line is not physically shorted to one side of the slot

on the ground plane. Instead of a physical short circuit, the microstrip feed line shown in Figure 1.3(a) extends approximately a quarter wavelength past the edge of the slot creating a virtual short circuit. A generic microstrip line as described in [4] can be used for this purpose, but the fan-like shape of the quarter-wave stub in Figure 1.3(a) aids in improving the bandwidth across which the stub is a virtual short circuit [10].

Figure 1.1: A slot antenna with a coaxial cable feed line and a "dyson-like" balun that is soldered to the ground plane [1].

Figure 1.2: A miniaturized slot antenna with a coaxial feed and a balun that is soldered to the ground plane [2].

Beyond the fabrication and size benefits of using a microstrip feed line, an argument must be made for the benefit of developing an analytical model to describe the coupling at the transition region between a microstrip feed line and a finite slot

(a) (b)

Figure 1.3: A (a) microstrip line feeding (b) a loaded slot antenna [3].

in a ground plane because the coupling behavior of this specific structure will be analyzed in depth in this thesis. The ability to accurately describe a discontinuity or transition in a microwave device using a mathematical model allows radio frequency engineers and antenna designers to implement a transmission line representation basis in the design of their system. With an analytical model, a transition in a microwave device can be described as a subsystem or block on their transmission line circuit such that an intuitive understanding of the system behavior based on circuit analysis techniques can achieved which aids in rapid system optimization. An analytical approach such as this allows for faster optimization of a system prior to simulating in a more time-consuming full wave solver like the High Frequency Structure Simulator (HFSS). A software like HFSS, which is based on Finite Element Method, is used in microwave system design to simulate a device before fabricating the device because it solves for pertinent structure parameters by enforcing Maxwell's equations and boundary conditions on an element-by-element basis [11]. The real world behavior prediction provided by full wave solver like HFSS, though it may require some computational time, ultimately saves time and reduces the cost of development for many microwave systems. These benefits are magnified if a less computationally intensive analytical model can optimize the system quickly before using a solver such as HFSS.

For the purpose of developing a model that can be expanded to vertical transitions between finite slots (or slot lines) and other types of transmission lines, the case of a microstrip-to-slot transition is considered above other transition types throughout this thesis. The existing models used to describe a microstrip-to-slot transition are explored where the slot is assumed to be finite. Analytical field models for common transmission line types such as microstrip line, strip line, and slot line are readily available [4]. Then by implementing other transmission line field models, this research can be expanded to apply to transitions between different types of transmission lines.

In microwave devices, a finite slot or aperture is often used as a radiating antenna element or to direct energy vertically from a feed line on one layer of a circuit to another. Researchers have employed many methods of describing the power transfer between a microstrip feed and a finite slot with little agreement between models. Some of these models are backed with rigorous theory that approach the computational complexity of a full wave solver like the High Frequency Electromagnetic Field Simulation Software (HFSS). The concept of field reciprocity has been a common theoretical backing for many existing theories. This research will explore the concept of reciprocity as well as a general coupling expression is laid out in [12]. Considering this previous work will help to build a basis upon which an improved model will be developed. This thesis proposes a novel approach to analytically model the coupling between a microstrip line feeding a finite slot in a ground plane. It attempts to alleviate the computational intensity of some previous methods of describing coupling between a microstrip and a slot while employing a more rigorous analysis than other simple closed-form analysis approaches.

In the end, this research provides a fundamental theoretical framework for models of vertical coupling between microstrip lines and finite apertures as well as other

types of printed planar feed lines such as strip lines and slot lines.

This thesis is structured such that some existing coupling models are introduced in Chapter 1. The equivalent circuit representations of some common models along with the concepts of Lorentz Reciprocity theory and general coupling theory are then introduced in Chapter 2. Additionally, it will be shown in Chapter 2 that the general coupling theory does not easily lend itself to an ideal transformer representation like the Lorentz Reciprocity Theorem approach claims [6]. Next an approach for defining the microstrip and slot electric fields is proposed and the concept of coupling as it is used in transformer theory and microwave filter design is recounted in Chapter 3. A transmission line equivalent circuit based on parallel mutual inductance and capacitance values in the transition region is proposed to aid in the optimization of these designs is also given in Chapter 3. The transition region in refers to the volume existing only inside a the dielectric material bounded by a microstrip conductor and a slot in the ground plane. The transition region has a width equal to the width of the microstrip line, a height equal to the height of the dielectric, and a length equal to the width of the slot line. The simulated and measured results for the developed theory describing the coupling in the transition region are given in Chapter 4 using input impedance and series coupling impedance metrics. Finally, concluding remarks and recommendations for future work are given in Chapter 5.

Chapter 2

Literature Review

This chapter introduces Lorentz Reciprocity Thoerem, General Coupling Theory, and three of the existing analytical models that have been developed to describe the coupling between a microstrip line and a slot line. The model proposed in Chapter 3 is unlike the previous models that will be discussed in this chapter and does not depend on an ideal transformer representation, but these models have been analyzed and inspected as a part of the initial literature review to inspect any complexities, oversimplifications, and ambiguities that may serve to show the trade-offs of employing other methods over the method proposed in this thesis.

2.1 Lorentz Reciprocity Theorem

Lorentz reciprocity is a concept derived from Faraday's Law and Ampere's law to relate the fields produced by independent sources within a region [4]. Consider the volume, V, depicted in Figure 2.1. Within the volume there exist two sets of sources that produce two sets of fields. $\bar{M}_1$ and $\bar{J}_1$ are magnetic and electric currents, respectively, which produce the electric field, $\bar{E}_1$, and the magnetic field, $\bar{H}_1$. Similarly, sources $\bar{M}_2$ and $\bar{J}_2$ produce the fields $\bar{E}_2$ and $\bar{H}_2$. Lorenz Reciprocity

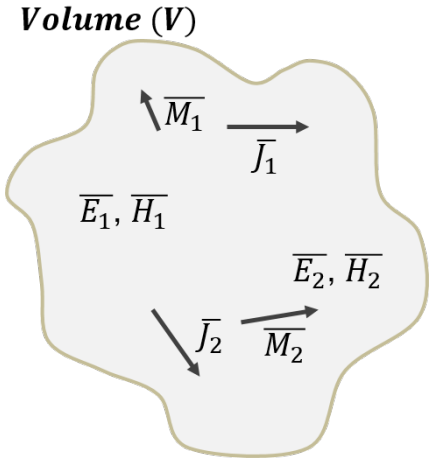

Figure 2.1: An example volume to demonstrate Lorentz Reciprocity Theorem similar to a depiction given in [4].

theorem relates these field and source vectors as

$$\nabla \cdot (\bar{E}_1 \times \bar{H}_2 - \bar{E}_2 \times \bar{H}_1) = \bar{J}_1 \cdot \bar{E}_2 - \bar{J}_2 \cdot \bar{E}_1 + \bar{M}_2 \cdot \bar{H}_1 - \bar{M}_1 \cdot \bar{H}_2. \quad (2.1)$$

In a sourceless region, this becomes

$$\nabla \cdot (\bar{E}_1 \times \bar{H}_2) = \nabla \cdot (\bar{E}_2 \times \bar{H}_1). \quad (2.2)$$

Furthermore, divergence theorem can be applied to describe the relationship between the independent fields in a sourceless region as

$$\oiint_S (\bar{E}_1 \times \bar{H}_2) \cdot d\bar{S} = \oiint_S (\bar{E}_2 \times \bar{H}_1) \cdot d\bar{S} \quad (2.3)$$

where S is the closed surface around the volume V.

2.2 Previous Work

Existing models for coupling through an aperture have been given in [5], [6], [13], [14], and [7]. Closed form expressions for the turns ratio of an ideal transformer to describe the coupling have been given in each of these models for the case of a microstrip conductor extending a quarter wavelength past an orthogonal finite slot or slotline in the ground plane. The turns ratio expressions in these papers do not agree exactly. This disagreement is a major motivation for research into an improved analytical model to describe the coupling between a microstrip line and a slot. This section introduces three existing models and mentions limitations of these models that motivate the research in this thesis.

2.2.1 Knorr Model

Knorr was among the first to compare a theoretical approach to describing the coupling at a transition between a microstrip line and a slot line to measured results [5]. He also compared theoretical results to measured results for the transition between a coaxial line and a slot line via a soldered transition such as the coax-to-slot transitions shown in Chapter 1. Though this model will be referred to as the Knorr model, the analytical model in [5] actually comes from a paper by Cohn [15]. Figure 2.2 shows a model of a slot-to-coax transition where the center conductor of the coax that reaches across the slot on the air side of the slot to be soldered is modelled as a half-circle conductor for mathematical convenience. This physical representation, shown in Figure 2.2 (a), allows for a simpler analytical model of L, the self inductance of the center conducting line, which is included in the equivalent circuit representation of the structure in Figure 2.2 (b) [5]. The equivalent circuit of the slot-to-coax transition contains an ideal transformer to represent the coupling be-

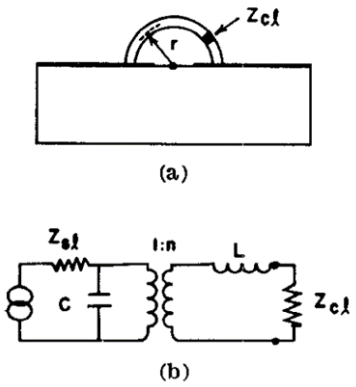

Figure 2.2: The (a) slotline to coax transition is modelled with a semi-circle representing the center pin of the coax extending across the slotline. An (b) equivalent circuit for the slot to coax transition is also given [5].

tween the coax and the slotline, a shunt capacitance that represents fringing effects at the end of the slot line feed, a slot line impedance, and a coaxial line impedance [5]. Figure 2.2 (b) shows the equivalent circuit of this transition assuming that a coaxial line is being fed with a slot line. A modified version of the equivalent circuit for the situation where a coaxial line is feeding a slot line is shown in Figure 2.3. Figure 2.4 shows a model of a slot-to-microstrip transition where the microstrip is

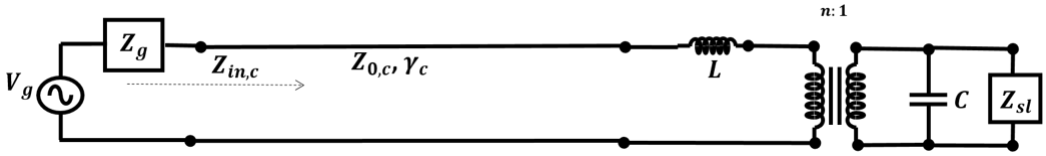

Figure 2.3: An interpretation of the Knorr model for a coaxial line feeding a finite slot.

assumed to be extending a quarter wavelength past the center of the slot line and the slot line is assumed to be extending a quarter wavelength past the center of the microstrip line. This is so that a virtual short can be assumed for both the perspective of the equivalent circuit where the slot line is feeding a microstrip line as in Figure 2.4 or for the perspective where the microstrip is feeding a slot line as in Figure 2.5.

In both equivalent circuits, the capacitance C_{oc} represents the fringing happening at the end of the microstrip line [5]. The reason that this capacitance can be included in the equivalent circuit in series is solely because of the virtual short created by the quarter-wavelength microstrip section extending past the center of the slot line. Figure 2.4 also shows a shunt reactance X_{sl} which represents the equivalent reactance due to a shorted slot [5]. Unlike Figure 2.4, Figure 2.5 assumes that the shorted end of the slot is ideal. This is an assumption that will carry through the remainder of this thesis, but may not be assumed by all of the presented previous work. Knorr's

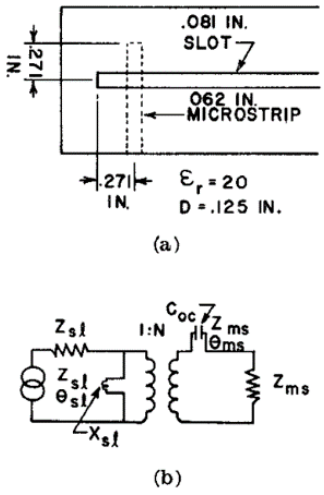

Figure 2.4: The (a) slotline to microstrip transition with the slotline extending a quarter wavelength past the microstrip and the microstrip line extending a quarter wavelength past the slotline as well as an (b) equivalent circuit to represent the structure [5].

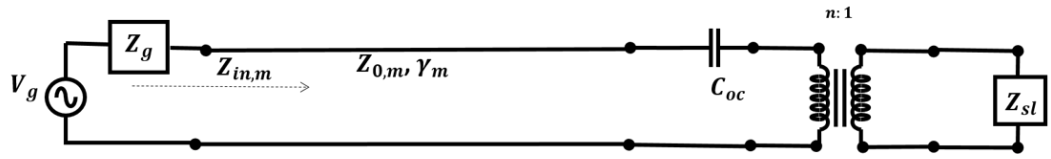

Figure 2.5: An interpretation of the Knorr model for a microstrip line coupled to a finite slot where the microstrip line extends a quarter wavelength past the slot.

model is based on the concept of an ideal transformer with a turns ratio that tends

to decrease linearly with frequency. Because of this, the behavior of the impedance looking into the ideal transformer from the perspective of the feedline in Figure 2.5 tends to follow the behavior of the slot input impedance except for a small magnitude decrease. This model was tested experimentally in [5] with a high permittivity material ($\epsilon_r = 20$). This was likely done because at high permittivities the fringing fields are tightly bound to the slot and the microstrip, which reduces radiation. This choice of permittivity aligns with the focus of [5] which is creating a good match between either a coaxial line and a slot line or a microstrip line and a slot line.

2.2.2 Das Model

This section briefly introduces a model developed in [6]. This model is an example of a computationally intensive full-wave approach to describe the coupling between a microstrip line and a slot line. The purpose of this thesis is to develop a simplified model that may work as a first step in optimizing a system before employing a method like the one given by Das in [6]. More important to the focus of this thesis is the transmission line equivalent circuit that is proposed in the top left corner of Figure 2.6. The equivalent circuit employs an ideal transformer to represent the power transfer at the region in the dielectric between a microstrip line and a slot line. In order to develop his model, Das uses current on each transmission line (in the case of a slot, the equivalent magnetic current is used) expressed as a summation of a travelling wave current and a standing wave current [6]. Das then uses the concept of reciprocity to relate the fields on the different coupled lines. The currents are used to express a relationship between the slot and microstrip fields. As a part of his work, Das provides a closed form expression to calculate the turns ratio of an ideal transformer representing the coupling between a slotline and a microstrip line

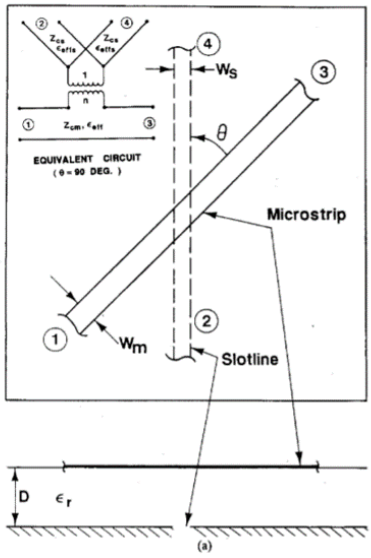

Figure 2.6: An example of a microstrip coupled to slot transition and an equivalent circuit representation using an ideal transformer given by Das (in the top left) [6].

that extends exactly one quarter wavelength past the slotline to create a virtual short-circuit. Das calculates his turns ratio for this specific case as being proportional to the square root of the ratio of the microstrip characteristic impedance to the slot characteristic impedance. He defines an expression for the turns ratio as

$$n = \frac{J_0(k_{es}W_m/2)J_0(k_{em}W_s/2)}{k_{es}^2 + k_{em^2}} \cdot \left[\frac{k_{em}^2 k_2 \epsilon_r}{k_2\epsilon_r cos(k_1 D) + k_1 sin(k_1 D)} + \frac{k_{es}^2 k_1}{k_1 cos(k_1 D) + k_2 sin(k_1 D)}\right] \tag{2.4}$$

where J_0 is the zeroth order Bessel function and k_1, k_2, k_{es}, and k_{em} are propagation coefficients defined in [6]. Figure 2.6 shows a depiction of a rotated slot fed with a microstrip line. The slot is rotated in Figure 2.6 in order to emphasize that his full model can account for any rotation of the slot with respect to the microstrip. If the slot is rotated, however, equation 2.4 could not be used because it is a simplified form of the analysis method presented in [6] for the strict case of a microstrip

oriented orthogonally to the length of the slot line and extending exactly a quarter wavelength past the edge of the slot line such that a virtual short is created. Equation 2.4 is not considered computationally intensive, but it is only useful for the strict orientation described. The full coupling analysis method given in [6] is complex and approaches the computational intensity of a full-wave solver. Next, we will introduce a more simplified existing model that is less computationally intensive than the Das model mentioned in this section.

2.2.3 Pozar Model

A method given in [7] employs the concept of reciprocity to model the coupling between a microstrip line and a finite slot in the ground plane. First, the propagating microstrip fields are described as a sum of forward and backward travelling waves according to the quasi-transverse electromagnetic model described in [4]. These fields, given in [7], are of the form

$$\bar{E} = \begin{cases} \bar{E}^+ + R\bar{E}^- \text{ for } y < 0 \\ \quad T\bar{E}^+ \text{ for } y > 0 \end{cases} \tag{2.5}$$

and

$$\bar{E} = \begin{cases} \bar{H}^+ + R\bar{H}^- \text{ for } y < 0 \\ \quad T\bar{H}^+ \text{ for } y > 0. \end{cases} \tag{2.6}$$

The transition region is described as having transmitted and reflected components according to the reflection coefficient R and the transmission coefficient T as shown in Figure 2.7. R, T, and the peak slot field magnitude V_0 are solved for by solving Lorentz reciprocity theorem in a sourceless region and enforcing the continuity

of the transverse magnetic field across the aperture. These values are solved for assuming the difference between the external and internal magnetic fields is expressed as a Greens function expression [7]. Depending on the slot field definition applied, multiple modes may be able to be achieved [7]. Using this approach, it was found that the coupling could be described in terms of a reflection coefficient which can be translated to a series impedance in the transmission line model of the system as shown in Figure 4.2. Following with the conclusion in [7], the coupling model given as a part of this research will assume that the coupling can always be described as a series impedance, Z, in a transmission line model as shown in Figure 4.2 where $Z_{in,end}$ is the input impedance looking in to the length of line extending past the center of the finite slot, V_g is the voltage supplied by the generator, Z_g is the generator impedance, $Z_{in,m}$ is the system input impedance at the generator, $Z_{0,m}$ is the characteristic impedance of the microstrip line feeding the finite slot, and $\gamma_m = \alpha + j\beta$ represents the losses and propagation constant along the microstrip line. This series impedance will be called the coupling impedance.

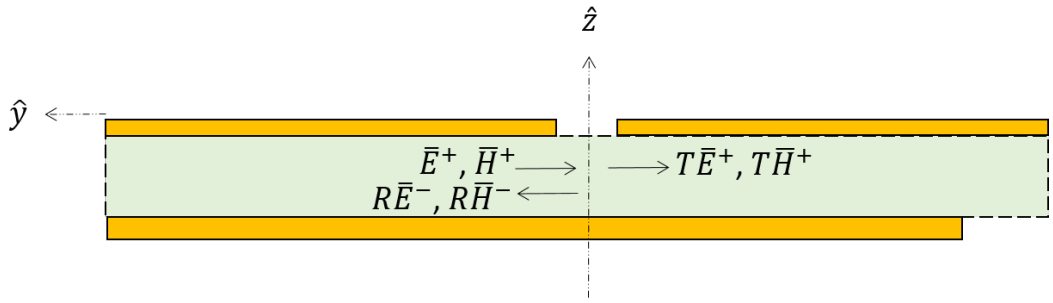

Figure 2.7: Visualization of the reflected and transmitted waves along a microstrip line that is coupled to a finite slot in the ground plane as described by Pozar in [7].

As a part of this work, a model for the electric field in the finite slot was given such

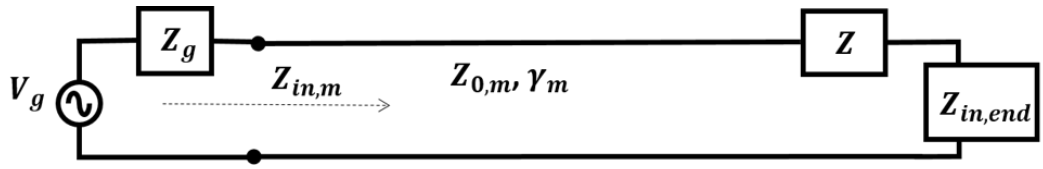

Figure 2.8: Equivalent circuit with a series coupling impedance, Z, to represent the coupling at the transition region between the microstrip conductor and the finite slot in the ground plane.

that

$$\bar{E}_y = \frac{\sin(k_e[\frac{L}{2} - |x|])}{W \sin(k_e \frac{L}{2})} \tag{2.7}$$

where

$$k_e = k_0 \sqrt{\frac{\epsilon_r + 1}{2}}. \tag{2.8}$$

In this field model, k_0 is the free space wave number, L is the length of the finite slot, W is the width of the slot, x is the dimension along which the field changes in magnitude, and ϵ_r is the reletivity of the dielectric material between the microstrip line and the slot line.

2.3 General Coupling Theory

General coupling theory is a concept that comes from the area of coupled resonator filter design. It is introduced here to clearly state the difference between the coupling coefficient used for resonant filter design purposes and the turns ratio that has often been included in equivalent circuits to describe the coupling between two systems. Beyond this, a relationship will be found between Lorentz Reciprocity Theorem and General coupling theory. This section serves as motivation for a po-

tential improved model that requires further research. Neither Lorentz Reciprocity theory nor General Coupling Theory have been implemented in the model proposed by this thesis because of ambiguities related to current and voltage definitions for the transition region. This ambiguity becomes clear in the Electric Coupling and Magnetic Coupling sections to follow.

The work in [12] gives an equation for the coupling coefficient between two coupled resonators based on their fields as

$$k = \frac{\iiint_V \varepsilon E_1 \cdot E_2 \, dV}{\sqrt{\iiint_V \varepsilon |E_1| \, dV \times \iiint_V \varepsilon |E_2|^2 \, dV}} + \frac{\iiint_V \mu H_1 \cdot H_2 \, dV}{\sqrt{\iiint_V \mu |H_1| \, dV \times \iiint_V \mu |H_2|^2 \, dV}}. \tag{2.9}$$

The coupling coefficient, according to this definition is a summation of the electric coupling coeffient and the magnetic coupling coeffient where the electric coupling coeffient is the ratio of the mutual stored electric energy between two structures normalized by the separate stored electric energies of the two structures prior to coupling. Similarly, the magnetic coupling coefficient is the ratio of the mutual stored magnetic energy between two structures normalized by the separate stored magnetic energies of the two structures prior to coupling. For an asynchronously tuned case (defined in [12]), the coupling coefficient can be written in terms of resonant frequencies as

$$k = \pm \left(\frac{f_{02}}{f_{01}} + \frac{f_{01}}{f_{02}} \right) \sqrt{\left(\frac{f_{p2}^2 - f_{p2}^2}{f_{p2}^2 + f_{p1}^2} \right)^2 - \left(\frac{f_{02}^2 - f_{01}^2}{f_{02}^2 + f_{01}^2} \right)^2} \tag{2.10}$$

where f_{01} and f_{02} are the separate resonant frequencies of two coupled structures and f_{p2} and f_{p1} are the characteristic frequency peaks of the coupled structure's transmission response. The relationship between stored energy and resonant fre-

quency makes sense because a structure is naturally resonant when the electric and magnetic stored energies are equal and opposite or at the frequency when the impedance of a reactive system becomes purely real [4]. The coupling coefficient given in [12] can not be used in place of a turns ratio for an ideal transformer to represent coupling between two structures. In the case of pure magnetic coupling, the turns ratio, n, of an ideal transformer, which is a voltage relationship, can be described in terms of the self impedance values, or self inductances in the case of an ideal transformer, of two different structures [16]:

$$n = \frac{V_{in}}{V_{out}} = \sqrt{\frac{L_m}{L_s}} \tag{2.11}$$

where V_{in} is the voltage at the input terminal of the ideal transformer, V_{out} is the voltage at the output terminal of the ideal transformer, L_m is the self inductance of the first coupled structure, and L_s is the self inductance of the second coupled structure [16]. According to [12], the coupling coefficient, k, of a magnetically coupled set of structures is defined as

$$k = \frac{M}{L_m L_s} \tag{2.12}$$

where M is the mutual inductance between L_m and L_s. Thus, for the magnetically coupled case, $k \neq n$. n and k can be related by

$$n = \frac{kL_m}{M}. \tag{2.13}$$

As noted previously, the concept of Lorentz Reciprocity has been used as a basis for the theory behind several coupling approaches in previous work. In this section, we will find a link between a non-conventional form of Lorentz Reciprocity Theorem

and the General Coupling theory.

2.3.1 Electric Coupling

Recall the following Maxwell's equations [4] for time harmonic fields:

$$\begin{aligned}
\nabla \times \bar{E}_1 &= -j\omega\mu\bar{H}_1 - \bar{M}_1 \\
\nabla \times \bar{H}_1 &= j\omega\epsilon\bar{E}_1 + \bar{J}_1 \\
\nabla \times \bar{E}_2 &= -j\omega\mu\bar{H}_2 - \bar{M}_2 \\
\nabla \times \bar{H}_2 &= j\omega\epsilon\bar{E}_2 + \bar{J}_2
\end{aligned} \tag{2.14}$$

Taking the complex conjugate of both sides of Maxwell's equations yields:

$$\begin{aligned}
\nabla \times \bar{E}_1{}^* &= -j\omega\mu\bar{H}_1{}^* - \bar{M}_1{}^* \\
\nabla \times \bar{H}_1{}^* &= j\omega\epsilon\bar{E}_1{}^* + \bar{J}_1{}^* \\
\nabla \times \bar{E}_2{}^* &= -j\omega\mu\bar{H}_2{}^* - \bar{M}_2{}^* \\
\nabla \times \bar{H}_2{}^* &= j\omega\epsilon\bar{E}_2{}^* + \bar{J}_2{}^*.
\end{aligned} \tag{2.15}$$

Two forms of Maxwell's equations have been presented. These expressions will be used in the derivation of an unconventional form Lorentz Reciprocity theorem that includes conjugated fields to describe mutual coupling.

Now take the dot product of the Faraday's Law listed in Equation 2.14 on both sides with $\bar{H}_2{}^*$ which yields

$$\bar{H}_2{}^* \cdot (\nabla \times \bar{E}_1) = \bar{H}_2{}^* \cdot (-j\omega\mu\bar{H}_1 - \bar{M}_1). \tag{2.16}$$

Equation 2.16 is simplified on the right hand side by the distributive property of the

dot product referenced in [17] such that

$$\bar{H_2}^* \cdot (\nabla \times \bar{E_1}) = \bar{H_2}^* \cdot (-j\omega\mu\bar{H_1}) - \bar{H_2}^* \cdot \bar{M_1}. \tag{2.17}$$

The cross product of $\bar{E_1}$ is expanded in terms of Cartesian components E_{1x}, E_{1y}, and E_{1z} as

$$\begin{aligned} \nabla \times \bar{E_1} &= \begin{bmatrix} \hat{x} & \hat{y} & \hat{z} \\ \dfrac{d}{dx} & \dfrac{d}{dy} & \dfrac{d}{dz} \\ E_{1x} & E_{1y} & E_{1z} \end{bmatrix} \\ &= \hat{x}\left(\frac{dE_{1z}}{dy}\frac{dE_{1y}}{dz}\right) - \hat{y}\left(\frac{dE_{1z}}{dx} - \frac{dE_{1x}}{dz}\right) + \hat{z}\left(\frac{dE_{1y}}{dx} - \frac{dE_{1x}}{dy}\right). \end{aligned} \tag{2.18}$$

Taking the dot product of $\bar{H_2}^*$ with Equation 2.18 results in

$$\begin{aligned} &\bar{H_2}^* \cdot (\nabla \times \bar{E_1}) = \\ &\bar{H_{2x}}^*\left(\frac{dE_{1z}}{dy} - \frac{dE_{1y}}{dz}\right) - \bar{H_{2y}}^*\left(\frac{dE_{1z}}{dx} - \frac{dE_{1x}}{dz}\right) + \bar{H_{2z}}^*\left(\frac{dE_{1y}}{dx} - \frac{dE_{1x}}{dy}\right). \end{aligned} \tag{2.19}$$

This is simplified further as

$$\begin{aligned} &\bar{H_2}^* \cdot (\nabla \times \bar{E_1}) \\ &= \bar{H_{2x}}^*\frac{dE_{1z}}{dy} - \bar{H_{2x}}^*\frac{dE_{1y}}{dz} - \bar{H_{2y}}^*\frac{dE_{1z}}{dx} + \bar{H_{2y}}^*\frac{dE_{1x}}{dz} + \bar{H_{2z}}^*\frac{dE_{1y}}{dx} - \bar{H_{2z}}^*\frac{dE_{1x}}{dy}. \end{aligned} \tag{2.20}$$

Then the right hand side of Equation 2.19 is substituted in to the left hand side of

equation 2.17 to give the relation

$$\begin{aligned}&\bar{H_{2x}}^{*}\frac{d\bar{E_{1z}}}{dy}-\bar{H_{2x}}^{*}\frac{d\bar{E_{1y}}}{dz}-\bar{H_{2y}}^{*}\frac{d\bar{E_{1z}}}{dx}+\bar{H_{2y}}^{*}\frac{d\bar{E_{1x}}}{dz}+\bar{H_{2z}}^{*}\frac{d\bar{E_{1y}}}{dx}-\bar{H_{2z}}^{*}\frac{d\bar{E_{1x}}}{dy}\\&=\bar{H_{2}}^{*}\cdot(-j\omega\mu\bar{H_{1}})-\bar{H_{2}}^{*}\cdot\bar{M_{1}}.\end{aligned}\tag{2.21}$$

Now take the dot product of the conjugated Ampere's law listed in Equation 2.15 with $\bar{E_1}$ to get

$$\bar{E_1}\cdot(\nabla\times\bar{H_2}^{*})=\bar{E_1}\cdot(j\omega\epsilon^{*}\bar{E_2}^{*}+\bar{J_2}^{*}).\tag{2.22}$$

Applying the same step leading to Equation 2.17, the distributive property is applied which simplifies Equation 2.22 to

$$\bar{E_1}\cdot(\nabla\times\bar{H_2}^{*})=\bar{E_1}\cdot(j\omega\epsilon^{*}\bar{E_2}^{*})+\bar{E_1}\cdot\bar{J_2}^{*}.\tag{2.23}$$

The cross product of $\bar{H_1}^{*}$ is expanded in terms of Cartesian components H^{*}_{2x}, H^{*}_{2y}, and H^{*}_{1z} as

$$\begin{aligned}\nabla\times\bar{H_2}^{*}&=\begin{bmatrix}\hat{x}&\hat{y}&\hat{z}\\\frac{d}{dx}&\frac{d}{dy}&\frac{d}{dz}\\H^{*}_{2x}&H^{*}_{2y}&H^{*}_{2z}\end{bmatrix}\\&=\hat{x}\left(\frac{dH^{*}_{2z}}{dy}\frac{dH^{*}_{2y}}{dz}\right)-\hat{y}\left(\frac{dH^{*}_{2z}}{dx}-\frac{dH^{*}_{2x}}{dz}\right)+\hat{z}\left(\frac{dH^{*}_{2y}}{dx}-\frac{dH^{*}_{2x}}{dy}\right).\end{aligned}\tag{2.24}$$

Taking the dot product of $\bar{E_1}$ with Equation 2.24 results in

$$\begin{aligned}&\bar{E_1} \cdot (\nabla \times \bar{H_2}^*) \\ &= \bar{E_{1x}}\left(\frac{dH^*_{2z}}{dy} - \frac{dH^*_{2y}}{dz}\right) - \bar{E_{1y}}\left(\frac{dH^*_{2z}}{dx} - \frac{dH^*_{2x}}{dz}\right) + \bar{E_{1z}}\left(\frac{dH^*_{2y}}{dx} - \frac{dH^*_{2x}}{dy}\right).\end{aligned} \tag{2.25}$$

This is simplified further as

$$\begin{aligned}&\bar{E_1} \cdot (\nabla \times \bar{H_2}^*) \\ &= \bar{E_{1x}}\frac{dH^*_{2z}}{dy} - \bar{E_{1x}}\frac{dH^*_{2y}}{dz} - \bar{E_{1y}}\frac{dH^*_{2z}}{dx} + \bar{E_{1y}}\frac{dH^*_{2x}}{dz} + \bar{E_{1z}}\frac{dH^*_{2y}}{dx} - \bar{E_{1z}}\frac{dH^*_{2x}}{dy}.\end{aligned} \tag{2.26}$$

Then the right hand side of Equation 2.26 is substituted in to the left hand side of equation 2.23 to give the relation

$$\begin{aligned}&\bar{E_{1x}}\frac{dH^*_{2z}}{dy} - \bar{E_{1x}}\frac{dH^*_{2y}}{dz} - \bar{E_{1y}}\frac{dH^*_{2z}}{dx} + \bar{E_{1y}}\frac{dH^*_{2x}}{dz} + \bar{E_{1z}}\frac{dH^*_{2y}}{dx} - \bar{E_{1z}}\frac{dH^*_{2x}}{dy} \\ &= \bar{E_1} \cdot (j\omega\epsilon^* \bar{E_2}^*) + \bar{E_1} \cdot \bar{J_2}^*.\end{aligned} \tag{2.27}$$

Now subtract equation 2.26 from equation 2.20 to get

$$\begin{aligned}&\bar{H_2}^* \cdot (\nabla \times \bar{E_1}) - \bar{E_1} \cdot (\nabla \times \bar{H_2}^*) \\ &= \bar{H_{2x}}^*\frac{dE_{1z}}{dy} - \bar{H_{2x}}^*\frac{dE_{1y}}{dz} - \bar{H_{2y}}^*\frac{dE_{1z}}{dx} + \bar{H_{2y}}^*\frac{dE_{1x}}{dz} + \bar{H_{2z}}^*\frac{dE_{1y}}{dx} - \bar{H_{2z}}^*\frac{dE_{1x}}{dy} \\ &- \left[\bar{E_{1x}}\frac{dH^*_{2z}}{dy} - \bar{E_{1x}}\frac{dH^*_{2y}}{dz} - \bar{E_{1y}}\frac{dH^*_{2z}}{dx} + \bar{E_{1y}}\frac{dH^*_{2x}}{dz} + \bar{E_{1z}}\frac{dH^*_{2y}}{dx} - \bar{E_{1z}}\frac{dH^*_{2x}}{dy}\right]\end{aligned} \tag{2.28}$$

Distributing the minus sign in the right hand side of Equation 2.28 changes the

expression to

$$\begin{aligned}
&\bar{H_2}^* \cdot (\nabla \times \bar{E_1}) - \bar{E_1} \cdot (\nabla \times \bar{H_2}^*) \\
&= \bar{H_{2x}}^* \frac{dE_{1z}}{dy} - \bar{H_{2x}}^* \frac{dE_{1y}}{dz} - \bar{H_{2y}}^* \frac{dE_{1z}}{dx} + \bar{H_{2y}}^* \frac{dE_{1x}}{dz} + \bar{H_{2z}}^* \frac{dE_{1y}}{dx} - \bar{H_{2z}}^* \frac{dE_{1x}}{dy} \\
&- \bar{E_{1x}} \frac{dH^*_{2z}}{dy} + \bar{E_{1x}} \frac{dH^*_{2y}}{dz} + \bar{E_{1y}} \frac{dH^*_{2z}}{dx} - \bar{E_{1y}} \frac{dH^*_{2x}}{dz} - \bar{E_{1z}} \frac{dH^*_{2y}}{dx} + \bar{E_{1z}} \frac{dH^*_{2x}}{dy}.
\end{aligned} \tag{2.29}$$

For comparison purposes that will be used later in this derivation, solve $\nabla \cdot (\bar{E_1} \times \bar{H_2}^*)$ to get

$$\begin{aligned}
&\nabla \cdot (\bar{E_1} \times \bar{H_2}^*) \\
&= \nabla \cdot \begin{bmatrix} \hat{x} & \hat{y} & \hat{z} \\ E_{1x} & E_{1y} & E_{1z} \\ H^*_{2x} & H^*_{2y} & H^*_{2z} \end{bmatrix} \\
&= \nabla \cdot [\hat{x}(E_{1y}H^*_{2z} - E_{1z}H^*_{2y}) - \hat{y}(E_{1x}H^*_{2z} - E_{1z}H^*_{2x}) + \hat{z}(E_{1x}H^*_{2y} - E_{1y}H^*_{2x})] \\
&= \frac{d}{dx}(E_{1y}H^*_{2z} - E_{1z}H^*_{2y}) - \frac{d}{dy}(E_{1x}H^*_{2z} - E_{1z}H^*_{2x}) + \frac{d}{dz}(E_{1x}H^*_{2y} - E_{1y}H^*_{2x}) \\
&= \frac{d}{dx}E_{1y}H^*_{2z} - \frac{d}{dx}E_{1z}H^*_{2y} - \frac{d}{dy}E_{1x}H^*_{2z} + \frac{d}{dy}E_{1z}H^*_{2x} + \frac{d}{dz}E_{1x}H^*_{2y} - \frac{d}{dz}E_{1y}H^*_{2x}.
\end{aligned} \tag{2.30}$$

The derivative chain rule is used to expand Equation 2.30 to get

$$\begin{aligned}
&\nabla \cdot (\bar{E_1} \times \bar{H_2}^*) \\
&= \frac{dE_{1y}}{dx}H^*_{2z} + \frac{dH^*_{2z}}{dx}E_{1y} - \frac{dE_{1z}}{dx}H^*_{2y} - \frac{dH^*_{2y}}{dx}E_{1z} \\
&- \frac{dE_{1x}}{dy}H^*_{2z} - \frac{dH^*_{2z}}{dy}E_{1x} + \frac{dE_{1z}}{dy}H^*_{2x} + \frac{dH^*_{2x}}{dy}E_{1z} \\
&+ \frac{dE_{1x}}{dz}H^*_{2y} + \frac{dH^*_{2y}}{dz}E_{1x} - \frac{dE_{1y}}{dz}H^*_{2x} - \frac{dH^*_{2x}}{dz}E_{1y}.
\end{aligned} \tag{2.31}$$

Compare the right hand sides of Equation 2.31 and Equation 2.29. These are equal, so it can be said that

$$\nabla \cdot (\bar{E}_1 \times \bar{H}_2{}^*) = \bar{H}_2{}^* \cdot (\nabla \times \bar{E}_1) - \bar{E}_1 \cdot (\nabla \times \bar{H}_2{}^*). \tag{2.32}$$

Then by substituting the right hand sides of Equation 2.17 and Equation 2.23 into the right hand side of Equation 2.32, the relation

$$\begin{aligned} &\bar{H}_2{}^* \cdot (\nabla \times \bar{E}_1) - \bar{E}_1 \cdot (\nabla \times \bar{H}_2{}^*) \\ &= \bar{H}_2{}^* \cdot (-j\omega\mu\bar{H}_1) - \bar{H}_2{}^* \cdot \bar{M}_1 - \bar{E}_1 \cdot (j\omega\epsilon^*\bar{E}_2{}^*) - \bar{E}_1 \cdot \bar{J}_2{}^* \\ &= -j\omega\mu\bar{H}_2{}^* \cdot \bar{H}_1 - \bar{H}_2{}^* \cdot \bar{M}_1 - j\omega\epsilon^*\bar{E}_1 \cdot \bar{E}_2{}^* - \bar{E}_1 \cdot \bar{J}_2{}^* \end{aligned} \tag{2.33}$$

can be made. The vector triple product rule given in [17] as $\nabla \cdot (\bar{A} \times \bar{B} = \bar{B} \cdot (\nabla \times \bar{A}) - \bar{A} \cdot (\nabla \times \bar{B})$ allows

$$\nabla \cdot (\bar{E}_1 \times \bar{H}_2^*) = \bar{H}_2^* \cdot (\nabla \times \bar{E}_1) - \bar{E}_1 \cdot (\nabla \times \bar{H}_2^*) \tag{2.34}$$

and

$$\nabla \cdot (\bar{E}_2 \times \bar{H}_1^*) = \bar{H}_1^* \cdot (\nabla \times \bar{E}_2) - \bar{E}_2 \cdot (\nabla \times \bar{H}_1^*) \tag{2.35}$$

to be true. Follow the same steps that were followed to arrive at Equation 2.33 by subtracting the simplified result of multiplying both sides of the second listed Maxwell's equation in Equation 2.15 with $\bar{E}_2$ from the simplified result of multiplying both sides of the third listed Maxwell's equation in Equation 2.14 with $\bar{H}_1^*$

to find that

$$\begin{aligned}
&\nabla \cdot (\bar{E}_2 \times \bar{H}_1^*) = \bar{H_1}^* \cdot (\nabla \times \bar{E}_2) - \bar{E}_2 \cdot (\nabla \times \bar{H_1}^*) \\
&= \bar{H_1}^* \cdot (-j\omega\mu\bar{H}_2) - \bar{H_1}^* \cdot \bar{M}_2 - \bar{E}_2 \cdot (j\omega\epsilon^*\bar{E_1}^*) - \bar{E}_2 \cdot \bar{J_1}^* \\
&= -j\omega\mu\bar{H_1}^* \cdot \bar{H}_2 - \bar{H_1}^* \cdot \bar{M}_2 - j\omega\epsilon^*\bar{E}_2 \cdot \bar{E_1}^* - \bar{E}_2 \cdot \bar{J_1}^*
\end{aligned} \tag{2.36}$$

is also true.

Let $\bar{J} = \bar{J}_s + \sigma\bar{E}$ and $\bar{J}^* = \bar{J}_s^* + \sigma^*\bar{E}^*$ to get

$$\begin{aligned}
\nabla \cdot (\bar{E}_1 \times \bar{H}_2^*) = -j\omega\mu(\bar{H}_1 \cdot \bar{H}_2^*) - \bar{M}_1 \cdot \bar{H}_2^* + j\omega\epsilon^*(\bar{E}_1 \cdot \bar{E}_2^*) - \bar{E}_1 \cdot \bar{J}_2^* = \\
-j\omega\mu(\bar{H}_1 \cdot \bar{H}_2^*) - \bar{M}_1 \cdot \bar{H}_2^* + j\omega\epsilon^*(\bar{E}_1 \cdot \bar{E}_2^*) - \bar{E}_1 \cdot \bar{J}_{2,s}^* - \sigma^*(\bar{E}_1 \cdot \bar{E}_2^*)
\end{aligned} \tag{2.37}$$

and

$$\begin{aligned}
\nabla \cdot (\bar{E}_2 \times \bar{H}_1^*) = -j\omega\mu(\bar{H}_1^* \cdot \bar{H}_2) - \bar{M}_1^* \cdot \bar{H}_2 + j\omega\epsilon^*(\bar{E}_1^* \cdot \bar{E}_2) - \bar{E}_2 \cdot \bar{J}_1^* = \\
-j\omega\mu(\bar{H}_1^* \cdot \bar{H}_2) - \bar{M}_1^* \cdot \bar{H}_2 + j\omega\epsilon^*(\bar{E}_1^* \cdot \bar{E}_2) - \bar{E}_2 \cdot \bar{J}_{1,s}^* - \sigma^*(\bar{E}_2 \cdot \bar{E}_1^*).
\end{aligned} \tag{2.38}$$

Apply a volume integral to both sides of Equation 2.37 and Equation 2.38 to get

$$\begin{aligned}
&\iiint_V \nabla \cdot (\bar{E}_1 \times \bar{H}_2^*) dV \\
&= -j\omega \iiint_V (\mu(\bar{H}_1 \cdot \bar{H}_2^*) - \epsilon^*(\bar{E}_1 \cdot \bar{E}_2^*)) dV \\
&- \sigma^* \iiint_V (\bar{E}_1 \cdot \bar{E}_2^*) dV - \iiint_V (\bar{M}_1 \cdot \bar{H}_2^* + \bar{E}_1 \cdot \bar{J}_{2,s}^*) dV
\end{aligned} \tag{2.39}$$

and

$$\begin{aligned}
&\iiint_V \nabla \cdot (\bar{E}_2 \times \bar{H}_1^*) dV \\
&= -j\omega \iiint_V (\mu(\bar{H}_1^* \cdot \bar{H}_2) - \epsilon^*(\bar{E}_1^* \cdot \bar{E}_2)) dV \\
&- \sigma^* \iiint_V (\bar{E}_2 \cdot \bar{E}_1^*) dV - \iiint_V (\bar{M}_1^* \cdot \bar{H}_2 + \bar{E}_2 \cdot \bar{J}_{1,s}^*) dV.
\end{aligned} \tag{2.40}$$

Divergence theorem says

$$\iiint_V \nabla \cdot (\bar{E}_1 \times \bar{H}_2^*) dV = \oiint_S (\bar{E}_1 \times \bar{H}_2^*) \cdot d\bar{S} \tag{2.41}$$

$$\iiint_V \nabla \cdot (\bar{E}_2 \times \bar{H}_1^*) dV = \oiint_S (\bar{E}_2 \times \bar{H}_1^*) \cdot d\bar{S} \tag{2.42}$$

It should be noted from the theory developed previously that a non-standard form of Lorentz reciprocity theorem can be stated as

$$\begin{aligned}
&\nabla \cdot (\bar{E}_1 \times \bar{H}_2^* - \bar{E}_2 \times \bar{H}_1^*) \\
&= \bar{H_2}^* \cdot (\nabla \times \bar{E}_1) - \bar{E}_1 \cdot (\nabla \times \bar{H_2}^*) \\
&- \bar{H_1}^* \cdot (\nabla \times \bar{E}_2) + \bar{E}_2 \cdot (\nabla \times \bar{H_1}^*) \\
&= -j\omega\mu \bar{H_2}^* \cdot \bar{H}_1 - \bar{H_2}^* \cdot \bar{M}_1 - j\omega\epsilon^* \bar{E}_1 \cdot \bar{E_2}^* - \bar{E}_1 \cdot \bar{J_2}^* \\
&+ j\omega\mu^* \bar{H_1}^* \cdot \bar{H}_2 + \bar{H_1}^* \cdot \bar{M}_2 + j\omega\epsilon \bar{E}_2 \cdot \bar{E_1}^* + \bar{E}_2 \cdot \bar{J_1}^*.
\end{aligned} \tag{2.43}$$

Then if $\bar{E}_1$, $\bar{E}_2$, $\bar{H}_1$, and $\bar{H}_2$ are all assumed to be real, then

$$\nabla \cdot (\bar{E}_1 \times \bar{H}_2^* - \bar{E}_2 \times \bar{H}_1^*) = \bar{J}_1 \cdot \bar{E}_2^* - \bar{J}_2^* \cdot \bar{E}_1 + \bar{M}_2^* \cdot \bar{H}_1 - \bar{M}_1 \cdot \bar{H}_2^*. \tag{2.44}$$

In a sourceless region this becomes

$$\nabla \cdot (\bar{E}_1 \times \bar{H}_2^*) = \nabla \cdot (\bar{E}_2 \times \bar{H}_1^*). \tag{2.45}$$

The form of the expressions $\frac{1}{2}\iint_S (\bar{E}_1 \times \bar{H}_2^*) \cdot d\bar{S}$ and $\frac{1}{2}\iint_S (\bar{E}_2 \times \bar{H}_1^*) \cdot d\bar{S}$ hints that these are terms that describe the a complex power flowing out of a surface similar to the integral of the complex Poynting vector mentioned in [4].

For the following theory, purely real harmonic fields and a purely real permittivity and permeability for the material are assumed. Similar to the derivation of Poynting's theorem in page 25-26 of [4], define from Equation 2.39 and the reciprocal Equation 2.40 the mutual complex power flowing out of the surface as

$$\begin{aligned} P_{o,m} &= \frac{1}{2}\iint_S (\bar{E}_1 \times \bar{H}_2^*) dS = \frac{1}{2}\iint_S (\bar{E}_2 \times \bar{H}_1^*) \cdot d\bar{S} \\ &= \frac{1}{2}\iint_S (\bar{E}_1 \times \bar{H}_2) dS = \frac{1}{2}\iint_S (\bar{E}_2 \times \bar{H}_1) \cdot d\bar{S}. \end{aligned} \tag{2.46}$$

Define the mutual power lost to heat as

$$\begin{aligned} P_{l,m} &= \frac{1}{2}\sigma^* \iiint_V (\bar{E}_1 \cdot \bar{E}_2^*) dV = \frac{1}{2}\sigma^* \iiint_V (\bar{E}_1^* \cdot \bar{E}_2) dV \\ &= \frac{1}{2}\sigma^* \iiint_V (\bar{E}_1 \cdot \bar{E}_2) dV = 0 \end{aligned} \tag{2.47}$$

which is equal to zero in the sourceless region if the material in the region has no conductivity.

Define the mutual electric and mutual magnetic stored energies as

$$\begin{aligned} W_{e,m} &= \frac{1}{4}\epsilon^* \iiint_V (\bar{E}_1 \cdot \bar{E}_2^*) dV = \frac{1}{4}\epsilon \iiint_V (\bar{E}_1^* \cdot \bar{E}_2) dV \\ &= \frac{1}{4}\epsilon \iiint_V (\bar{E}_1 \cdot \bar{E}_2) dV. \end{aligned} \tag{2.48}$$

and

$$W_{m,m} = \frac{1}{4}\mu \iiint_V (\bar{H}_1 \cdot \bar{H}_2^*) dV = \frac{1}{4}\mu^* \iiint_V (\bar{H}_1^* \cdot \bar{H}_2) dV$$
$$= \frac{1}{4}\mu \iiint_V (\bar{H}_1 \cdot \bar{H}_2) dV, \tag{2.49}$$

respectively. Define the mutual complex power delivered by the sources as

$$P_{s,m} = -\frac{1}{2} \iiint_V (\bar{M}_1 \cdot \bar{H}_2^* + \bar{E}_1 \cdot \bar{J}_{2,s}^*) dV = -\frac{1}{2} \iiint_V (\bar{M}_1^* \cdot \bar{H}_2 + \bar{E}_2 \cdot \bar{J}_{1,s}^*) dV$$
$$= -\frac{1}{2} \iiint_V (\bar{M}_1 \cdot \bar{H}_2 + \bar{E}_2 \cdot \bar{J}_{1,s}) dV = 0 \tag{2.50}$$

which is equal to zero because a sourceless region is being considered. If a sourceless region is not being considered then a definition for $P_{s,m}$ can be derived from Equation 2.43. For the purpose of describing coupling between a microstrip line and a slot, the volume V of the above equations could be considered to be the transition region volume depicted in Figure 2.9.

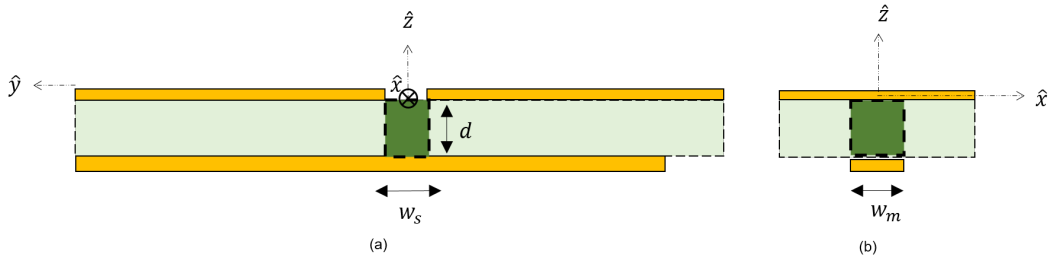

Figure 2.9: Depiction of the transition region extending across the width of the slot, w_s, the width of the microstrip conductor, w_m, and the hight of the dielectric d for a microstrip line coupled to a slot (a) along the length of the microstrip line and (b) from the front cut plane of the microstrip line.

Thus, it can be said that

$$P_{s,m} = P_{o,m} + P_{l,m} + 2j\omega(W_{m,m} - W_{e,m}). \tag{2.51}$$

For the considered sourceless region, this becomes

$$P_{o,m} = 2j\omega(W_{e,m} - W_{m,m}). \tag{2.52}$$

Finally, [4] gives a relation such that the energy stored in a parallel plate capacitor is

$$W_e = \frac{1}{2}C|\bar{V}|^2_{avg} = \frac{1}{4}C|\bar{V}|^2 \tag{2.53}$$

where W_e is stored electric energy, C is the capacitance of the parallel plate capacitor, and V is the voltage difference across the plates of the parallel plate capacitor. The definition for the mutual stored electric energy $W_{e,m}$ was developed in Equation 2.48 so Equation 2.53 can be used to develop a definition for the mutual capacitance C_m in a sourceless region with two sets of fields as

$$\frac{1}{4}C_m|\bar{V}|^2 = \frac{1}{4}\epsilon \iiint_V (\bar{E}_1 \cdot \bar{E}_2)dV. \tag{2.54}$$

The stored electric energies $W_{1,e}$ and $W_{2,e}$ of electric fields 1 and 2 can be related separately as

$$\frac{1}{4}C_1|\bar{V}|^2 = \frac{1}{4}\epsilon \iiint_V |\bar{E}_1|^2 dV \tag{2.55}$$

and

$$\frac{1}{4}C_2|\bar{V}|^2 = \frac{1}{4}\epsilon \iiint_V |\bar{E}_2|^2 dV. \tag{2.56}$$

Define the mutual capacitance C_m to be

$$C_m = \frac{\epsilon \iiint_V (\bar{E}_1 \cdot \bar{E}_2) dV}{|V|^2}. \tag{2.57}$$

The energies stored separately in each independent set of fields is

$$C_1 = \frac{\epsilon \iiint_V |\bar{E}_1|^2 dV}{|V|^2} \tag{2.58}$$

$$C_2 = \frac{\epsilon \iiint_V |\bar{E}_2|^2 dV}{|V|^2} \tag{2.59}$$

This agrees with the definition of the coupling coefficient k_e for electric coupling case given in [12] as

$$k_e = \frac{C_m}{C_1 C_2} = \frac{W_{m,e}}{W_{1,e} W_{2,e}} = \frac{\iiint_V \epsilon E_1 \cdot E_2 dV}{\sqrt{\iiint_V \epsilon |E_1|^2 dV \times \iiint_V \epsilon |E_2|^2 dV}}. \tag{2.60}$$

A difficulty with using the derived mutual capacitance, C_m, to describe the coupling between two structures like a microstrip and a slot appears with the definition of the voltage, V. C_m is found for a volume without a set voltage difference V across two points such that it could be implemented with ease in a circuit model.

2.3.2 Magnetic Coupling

For magnetic coupling,

$$W_{m,m} = \frac{1}{4}L_m|I|^2 = \frac{1}{4}\mu \iiint_V (\bar{H}_1 \cdot \bar{H}_2^*)dV = \frac{1}{4}\mu \iiint_V (\bar{H}_1^* \cdot \bar{H}_2)dV$$
$$= \frac{1}{4}\mu \iiint_V (\bar{H}_1 \cdot \bar{H}_2)dV \tag{2.61}$$

assuming again a sourceless region with purely real fields in a material with a real permittivity and permeability. Define the mutual inductance L_m to be

$$L_m = 4\frac{W_{m,m}}{|I|^2} = 4\frac{\iiint_V \mu H_1 \cdot H_2 dV}{|I|^2} \tag{2.62}$$

based on the definition of the stored energy in an inductor [4].

Similarly, the stored magnetic energy $W_{m,1}$ and $W_{m,2}$ of the separate fields can be defined as

$$W_{m,1} = \frac{1}{4}L_1|I|^2 \tag{2.63}$$

and

$$W_{m,2} = \frac{1}{4}L_2|I|^2, \tag{2.64}$$

respectively.

Thus a coupling coefficient that agrees with the coupling coefficient for the magnetically coupled case in [12] can be defined as

$$k_m = \frac{L_m}{L_1 L_2} = \frac{W_{m,m}}{W_{m,1}W_{m,2}} = \frac{\iiint_V \mu H_1 \cdot H_2 dV}{\sqrt{\iiint_V \mu|H_1|^2 dV \times \iiint_V \mu|H_2|^2 dV}} \tag{2.65}$$

Similar to the Electric Coupling case, a difficulty with using the derived mutual inductance, L_m, to describe the coupling between two structures appears with the definition of the current, I. This is because the mutual energy is found for a volume without a single set current direction as in an inductor. This ambiguity makes it difficult to use the mutual inductance definition in a circuit model representation.

2.3.3 Conclusions about Previous Work

It has been shown that elements of the General Coupling theory can be traced back to the Lorentz Reciprocity theorem, Maxwell's Equations, and Poynting's Theorem. The coupling coefficients for electric coupling and magnetic coupling proposed by general coupling theory are a ratio of coupled energy to stored energy which can be linked to the resonant frequencies of two coupled resonators. In [7], Pozar uses the concept of Lorentz Reciprocity, the boundary condition related continuity of the tangential component of the magnetic field across a boundary, and a Green's Function field model to develop an expression for a reflection coefficient R which can be used to describe the series coupling impedance Z in a transmission line model. In [6], Das employs Lorentz reciprocity in a time-time intensive full wave technique. In [5], the coupling coefficient is provided using a method first proposed by Cohn in [15]. In general, the models that have been introduced in this chapter do not agree as will be shown in Chapter 4. This disagreement between existing models is a leading reason for why more research is required to find an accurate coupling model for the vertical transition between a microstrip feed line and a finite slot in a ground plane.

In order to develop a novel analytical coupling model using the concept of reciprocity, a field model must be developed for two separate structures: the microstrip

and the slot. Next, an equivalent circuit should be proposed to describe the coupling such that it can be used in a transmission line model of the system. The field models that will be used and an improved coupling equivalent circuit will be proposed in Chapter 3. These field models are different than the field models used by Pozar in [7]. The model developed in Chapter 3 is less computationally intensive than the model proposed by Das in [6], employs a simplified circuit analysis technique that rivals the simplicity of the model proposed by Pozar, and rivals the accuracy of both the model given by Knorr in [5] and the closed form expression for the case of a virtual short circuit transition given by Das in [6].

Chapter 3

Methodology

The previous work of Knorr, Das, and Pozar was introduced in Chapter 2 as they relate to the coupling between a microstrip and a slot. All of this work depends, in some form, on a relationship between the fields on a microstrip line and the fields on a slot line. Thus, in this chapter a model for the fields on the microstrip line will be introduced in Section 3.1 and a model for the fields that can exist on a finite slot will be given in Section 3.2. In all of the previous work introduced in Chapter 1, researchers assumed that the coupling could be described in terms of a turns ratio, n. In section 3.3 the difference between the turns ratio n and the coupling coefficient definitions k_e and k_m from General Coupling Theory that were given in Chapter 2 will be shown. In Section 3.4, a modified equivalent circuit based on a definition of mutual inductance and mutual capacitance that differs from the definitions of mutual inductance and capacitance based on mutually stored energy as given in Chapter 2 such that the required parameters can be clearly defined is presented. The values are calculated such that they depend on aligning field components, which is a concept borrowed from the definition of mutually stored energy in Sections 2.3.1 and 2.3.2. This modified equivalent circuit and associated value calculations serve as the the improved model suggested by this thesis. This model will be tested in Chapter 4.

3.1 Analytical TEM Microstrip Field Model

The microstrip line and the slot in the ground plane are considered as separate structures with separate power sources. The coupling at the transition region in the dielectric material above the microstrip conductor and below the slot in the ground plane can be described using field representations for the microstrip and for the slot. Thus, in order to analyze mutual coupling effects between fields produced by separate sources at the transition region between the slot and the microstrip line, the independent fields produced by each separate structure must be modelled. In this section, the analytical field model that will be used to describe the coupling in the improved coupling model given in Section 3.4 will be introduced. Figure 3.1 shows the front cut plane of a microstrip line. Figure 3.2 shows a representation of a typical electric field orientation on a microstrip line, including fringing fields. Figure 3.3 shows the electric and magnetic field orientations under a transverse electromagnetic (TEM) field assumption where the fringing is taken into account in the form of an effective permittivity defined in [4] as

$$\epsilon_{eff} = \frac{\epsilon_r + 1}{2} + \frac{\epsilon_r - 1}{2} \frac{1}{\sqrt{1 + 12\frac{d}{w_m}}}. \tag{3.1}$$

The microstrip field is modelled using the quasi-transverse electromagnetic approximation for the microstrip line as given in [4]. However, because the microstrip conductor consists of a finite substrate with a ground plane on one side and a conducting line on the other, some of the electric field lines generated by the microstrip reach outside of the substrate into the air such that the phase matching condition in either material (dielectric or air) is violated [4]. An effective dielectric constant is required to describe the material during microstrip operation to account for the

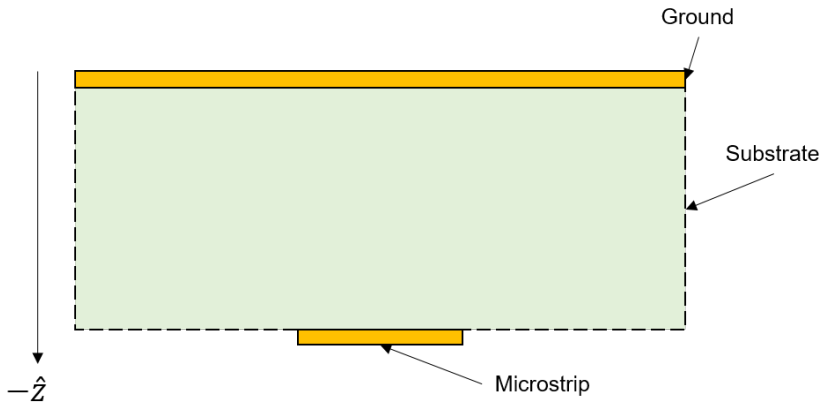

Figure 3.1: Front cut plane of a microstrip line.

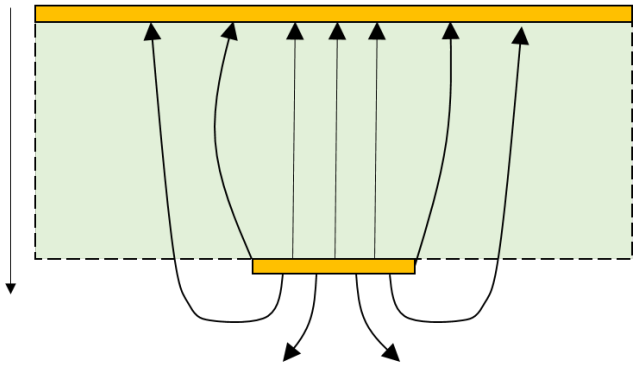

Figure 3.2: Depiction of some typical microstrip fringing electric field behavior as seen from the front cut plane of a microstrip line.

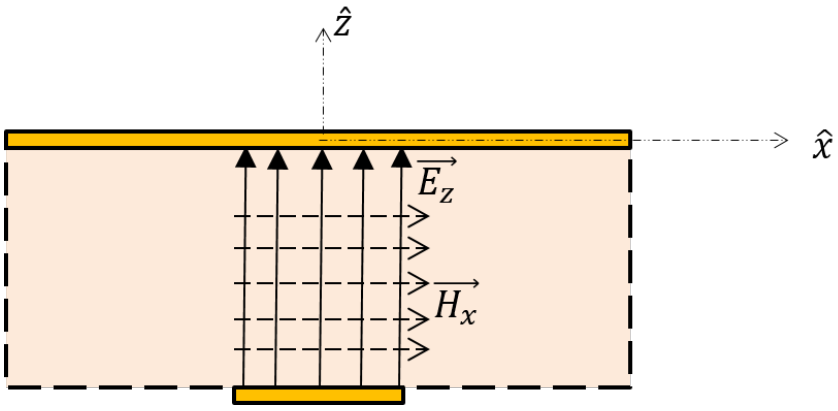

Figure 3.3: Electric and magnetic field orientation for the quasi-TEM microstrip field model.

fringing fields that reach into the air. This effective dielectric constant is frequency dependent. The frequency dependency of the effective dielectric constant is taken into account by an approximation given in [18]. The TEM model was chosen to represent the microstrip line because the model is focused on improving practical microwave structure modelling where the dielectric thickness is much smaller than the wavelength where the quasi-TEM approximation is valid [4]. The quasi-TEM approximation for the microstrip line only takes into account one possible mode that can appear on the line. At high frequencies, higher order modes are likely to appear on the line [4]. Thus it may be argued that models which take higher order modes into account are more rigorous than the model proposed in this research for high frequencies. The frequencies analyzed in this thesis have been chosen so that they exist below X-band so the quasi-TEM approximation is adequate [19]. The generator voltage of the system is assumed to be $V_g = 1\text{V}$ so the peak voltage for the quasi-TEM voltage wave travelling down the microstrip is assumed to be normalized to

$$V_0 = V_g \frac{Z_{in}}{Z_{in} + Z_g} = \frac{Z_{in}}{Z_{in} + Z_g}. \tag{3.2}$$

by applying a voltage divider to the equivalent circuit shown in Figure 3.4 where

$$Z_{in} = Z_{0,m} \frac{e^{\gamma_m l_m} + \Gamma_0 e^{-\gamma_m l_m}}{e^{\gamma_m l_m} - \Gamma_0 e^{\gamma_m l_m}} \tag{3.3}$$

is the input impedance looking in to the microstrip line that depends on the propagation constant and attenuation, $\gamma_m = \alpha + j\beta$, along the length of the line, l_m,

and

$$\Gamma_0 = \frac{Z_l - Z_{0,m}}{Z_l + Z_{0,m}} \tag{3.4}$$

is the reflection coefficient at the end of the microstrip line where Z_l is the load impedance [4]. For the case of an open microstrip line, Z_l can be determined using a method given in [18]. The generator impedance, Z_g is assumed to be equal to the characteristic impedance of the microstrip line $Z_{0,m}$. Then the voltage along the microstrip line can be found using the quasi-TEM model given in [4] as

$$V = V_0(e^{\gamma_m y} + \Gamma_0 e^{-\gamma_m y}) \tag{3.5}$$

and the current can be found as by employing the relation $I_0 = \frac{V_0}{Z_{0,m}}$ as

$$I = I_0(e^{\gamma_m y} - \Gamma_0 e^{-\gamma_m y}). \tag{3.6}$$

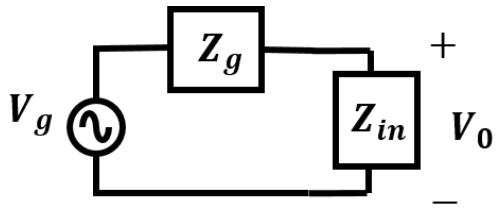

Figure 3.4: Equivalent circuit to aid in the calculation of V_0.

An important addition to the TEM approximation of equation 3.9 is that $\gamma_m = \alpha + j\beta$ has been assumed to have a lower β in the slot transition region compared to the rest of the line. $\beta = \frac{2\pi}{\lambda'}$ where λ' can be estimated using an expression from

[20] in terms of a modified effective wavelength of the microstrip line as

$$\lambda' = \lambda_{eff}[1 + \frac{1}{8\pi}(\frac{w_s}{w_m})^2 \frac{\lambda_{eff}^2}{w_m d}]. \tag{3.7}$$

This is assuming that the effective wavelength of the microstrip line is

$$\lambda_{eff} = \frac{c}{f\sqrt{\epsilon_{eff}}} \tag{3.8}$$

where c is the speed of light, f is the frequency, and ϵ_{eff} is the effective permittivity of the microstrip line defined in Equation 3.1. It is also assumed from [4] that only dielectric losses are taken into account and that the conductor losses are negligible such that

$$\alpha = \alpha_d = k_0 \epsilon_r (\epsilon_{eff} - 1) \frac{tan(\delta)}{2\sqrt{\epsilon_{eff}(\epsilon_r - 1)}} \tag{3.9}$$

where k_0 is the free space wave number and $tan(\delta)$ is the dielectric loss tangent. Conductor losses are assumed to be negligible because the test scenarios in Chapter 4 are fabricated using copper-plated materials. Because of the high conductivity of copper, the conductor loss can be assumed to be negligible according to a method for calculating conductor loss that is given in [4]. Next, the electric field along the length of the microstrip line can be defined similar to a definition for the slot electric field in [1] as

$$E_{microstrip} = E_z = \frac{V}{d} \tag{3.10}$$

where d is the thickness of the substrate. This parallel plate assumption can be made because of the assumed constant field orientation of the quasi-TEM electric

field model. The field is $\hat{z}$ directed according to the axis shown in Figure 3.3. Because of this the magnetic field is assumed to have a single component H_x in the $\hat{x}$ direction that varies in the $\hat{y}$ direction. The magnitude of the magnetic flux density is calculated using Maxwell's equations. Recall that

$$\nabla \times \bar{E} = -j\omega\mu\bar{B} \tag{3.11}$$

where $\bar{E} = E_z$ is the electric field on the microstrip line. Since E_z varies along the $\hat{y}$ direction only, the magnetic field can be calculated by evaluating

$$B_x = -\frac{1}{jw}\frac{d}{dy}E_z \tag{3.12}$$

such that the magnetic field is $H_x = \dfrac{1}{\mu}B_x$ where μ is the permeability of the substrate between the slot and the microstrip. The transition region between the microstrip line and the slot line is defined as the volume reaching across the width of the microstrip line (w_m), the width of the slot line (w_s), and the height of the dielectric (d) as shown in Figure 3.5.

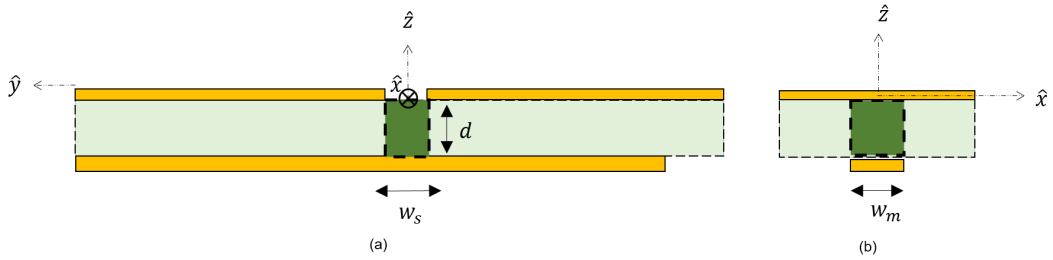

Figure 3.5: Depiction of the transition region for a microstrip line coupled to a slot (a) along the length of the microstrip line and (b) from the front cut plane of the microstrip line.

The fields at the transition region do not behave in the predictable behavior that has been described for a TEM line in [4]. When an aperture is introduced to the

system, the electric field lines can no longer be modelled as being only $\hat{z}$ directed because the field lines adapt to reach for conducting surfaces. This assumption is based on underlying physical properties of conductive materials. Thus, the $\hat{z}$ directed electric field lines depicted in Figure 3.6 (a) have been perturbed for the purpose of this research to extend only towards the conductors as shown in Figure 3.6 (b) in the transition region between the microstrip and the slot. For mathematical simplicity, the electric fields are assumed to make a linear slant as shown in Figure 3.6(b). In reality, the fields are not so simple. A curved field should be expected for these fringing fields at the slot edges, but further research is required to fully understand this fringing field behavior. Under the slanted field assumption, the electric field lines at the transition region can be said to have $\hat{z}$ and $\hat{y}$ directed components. For simplicity, the field direction has been assumed to slope linearly from the microstrip conductor to either edge of the slot. In reality, the fringing effects may have curved behaviors that vary with frequency and material properties.

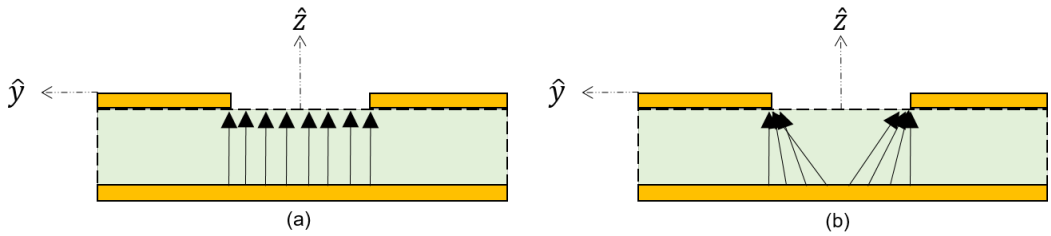

Figure 3.6: Field perturbation to model electric field orientation when a slot exists in the ground plane.

3.2 Analytical Slot Field Model

The slot fields are derived in [1] and take into account higher order modes of the slot line. An example of the first order mode of the electric field is shown in Figure

3.7 and some examples of higher order modes as the slot increases in length are shown in Figure 3.8. Figure 3.8 compares the Ruyle method given in [1] to the finite slot field approximation given by Pozar in [7]. It shows that the Ruyle method is more robust to changes in the length of the finite slot. To derive the slot fields, an approximate slot characteristic impedance and slot wavelength is calculated using closed from expressions listed in [19] and [21] based on curve fitting techniques. This characteristic impedance is used as a first guess in an iterative method given by Cohn in [15] which finds a more accurate characteristic impedance starting at this first guess. The slot wavelength is an effective wavelength for the slot that depends on the permittivity of the materials around the slot. This wavelength tends to be much smaller than the free-space wavelength which results in fields that are closely confined to the slot [15]. Since the structure we are looking at is a radiating finite slot on a finite ground plane, it is useful to note that radiation loss tends to increase with a lower permittivity and a higher slot wavelength [15]. The characteristic

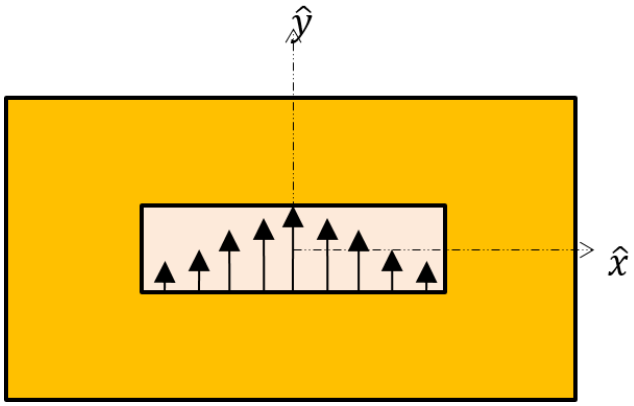

Figure 3.7: Depiction of typical electric field vectors for first mode of the finite slot.

impedance and slot wavelength values obtained from [19] and [21] are used as initial approximations for an iterative technique for refining the slot wavelength and slot characteristic impedance values given in [15]. Thus, even if the permittivity

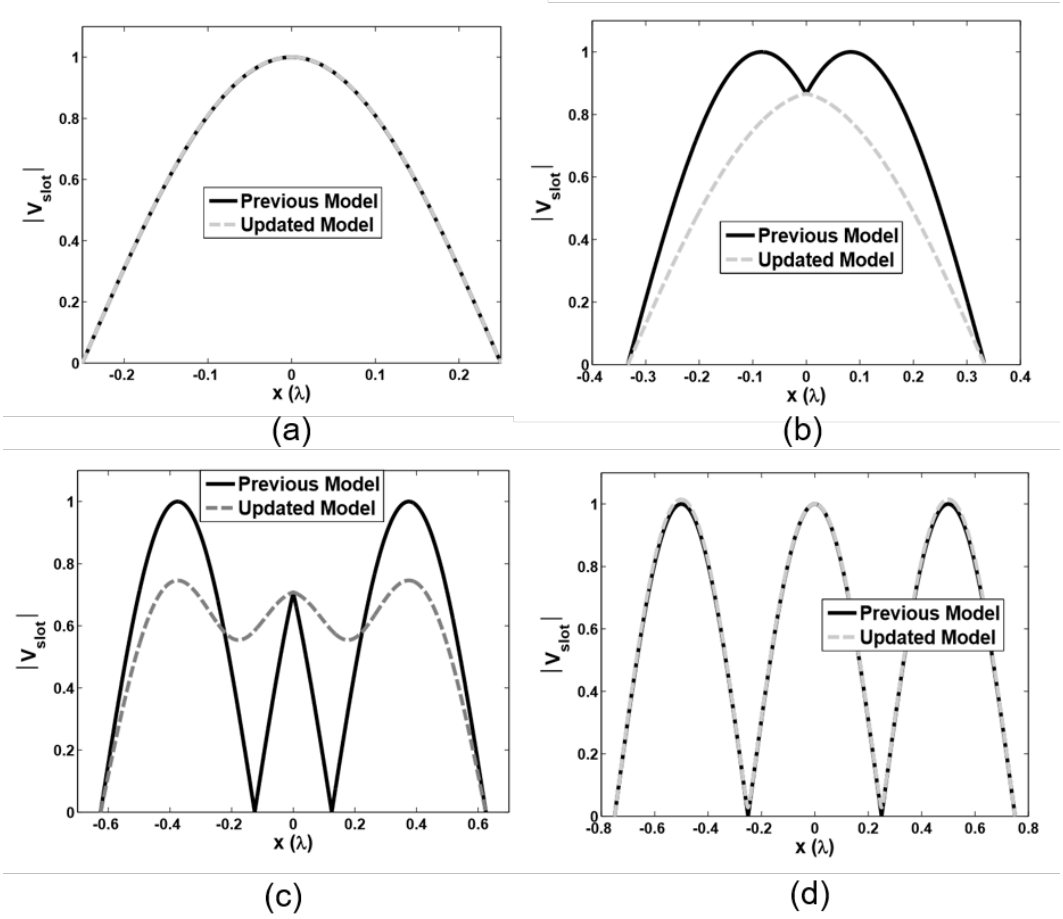

Figure 3.8: Example of field magnitudes for multiple modes as slot increases in size [1].

and dimension restrictions in [19] and [21] are violated, a useable slot characteristic impedance and slot wavelength can still be found. The iterative method given in [15] assumes some physical design approximations which should not be violated if a system designer wishes to employ the method: $\frac{w_s}{\lambda} << 1$, $\frac{w}{b} <= 0.15$, $w < \frac{\lambda}{4\sqrt{\epsilon_r}}$, and $w <= d$ [15]. Where $b = 1.2\lambda_s$ has been assigned and is the distance perpendicular to the slot length where either electric or magnetic walls are placed in parallel to the slot as a part of the method. The slot characteristic impedance is calculated in [15] is defined as $Z_0 = \frac{V^2}{2P}$ where $V = -\int E_y dy$ is

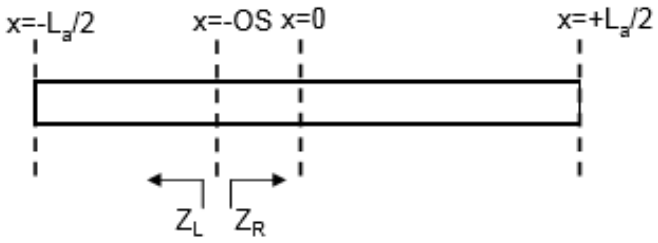

Figure 3.9: Depiction of slot input impedance looking left Z_l and right Z_r inside the finite slot [1].

described as being the voltage amplitude across the slot and P is described as being the average power flow of the wave. According to [15], the slot characteristic impedance approximation can be inaccurate when a designer tries to match to another type of line. For example, matching a slot to a 50 ohm microstrip line can require up to a 75 ohm slot line characteristic impecance [15]. This happens perhaps because of reactive discontinuity effects [15] that may result from an abrupt transition such as the coupling transition that is analyzed in this thesis.

Once the characteristic impedance and the slot wavelength have been approximated using the method in [15], the electric field inside the slot can be calculated using the method given in [1]. As a part of this method, the input impedance of the slot in the ground plane is described as a parallel combination of the input impedance looking to the left and to the right of the slot as shown in Figure 3.9 [1]. The impedances looking to the left and the right are calculated using transmission line theory. In order to do this, the attenuation and propagation constant of the slot line are found, in part, using the dielectric loss tangent and the slot effective wavelength [1]. The electric field on the slot is also found using transmission line theory to find the voltage on the line and the relation $\bar{E} = \dfrac{V}{w_s}$ [1]. Thus, multiple modes are taken into account on the line. If antenna performance was of interest,

the power radiated can be derived based on the equivalence principle wherein the electric field can be converted to a magnetic current from which far-field electric fields can be approximated [1].

The electric field in the slot is $\hat{y}$ directed with reference to Figure 3.7. Thus, the $\hat{x}$ directed magnetic field can be found by employing Maxwell's equations. The magnetic field can be found from the electric field according to

$$\nabla \times \bar{E} = -j\omega\mu\bar{B} \tag{3.13}$$

as was used in the quasi-TEM microstrip field model. The difference in this case is that the electric field $\bar{E} = E_y$ has a single component in the $\hat{y}$ direction that varies along the $\hat{x}$ direction such that Equation 3.15 can be evaluated to be

$$\bar{H_x} = \frac{-1}{j\omega\mu}\frac{dE_y}{dy}. \tag{3.14}$$

Magnetic fringing fields are taken into account in the substrate according to [22] such that H_x and H_z vary with $\hat{y}$ and $\hat{z}$. The slot fringing electric fields can be found using

$$\nabla \times \bar{H} = j\omega\epsilon\bar{D} \tag{3.15}$$

assuming a sourceless region. The fringing electric field components that result from the above relation are E_z and E_x components that both vary in the $\hat{y}$ and $\hat{z}$ directions. For the purpose of reducing the computational intensity of the model that will be proposed in Section 3.4 of this chapter, the fringing electric fields may be assumed to be constant across the $\hat{z}$ direction in some cases. It will be shown in Section 4.2.5 that this assumption of a constant fringing field can cause errors such

as adding extra resonances to the predicted coupling impedance of a system.

3.3 Ideal Transformer

The concept of coupling is used in ideal transformer theory. An ideal transformer transfers energy using the changing magnetic field on one conductor to induce a voltage onto a second conductor [23]. Often times, a number of coils on either conductor allows control over the amount of current induced on the second conductor and a ferromagnetic core is used to direct the magnetic field to the location of the second coil due to its extremely high permeability [23]. Based on its shape, it also changes the direction of the magnetic field from one side to the other such that the current coming out of the transformer and the voltage coming out of the transformer has the same polarity as the input voltage and current depending on the direction the coils are wrapped. Ideally, the power into the system is equal to the power out and the ratio of voltage or current in to the voltage or current out is equal to the ratio of the number of turns on the first coil to the number of the turns on the second coil [23]. This ratio is called the turns ratio or coupling coefficient. Thus for an ideal transformer, the coupling coefficient is described as $n = \frac{V_{in}}{V_{out}}$. Figure 3.10 shows a transmission line model of a finite slot coupled to a microstrip feed line. This model for the transition is employed by Knorr in [5] and Das in [6] with different definitions for the turns ratio n. The series coupling impedance, Z, shown in Figure 4.2 is an equivalent circuit approach that was reinforced by Pozar in [7]. The transmission line equivalent circuit that uses a series coupling impedance representation for the coupling that occurs at the transition region between the microstrip and the slot and inside the dielectric material can be seen in Figure 4.2. The coupling impedance is equal to the input impedance, Z_{in}, of the ideal transformer shown in Figure 3.12,

which is a section of the system transmission line representation shown in Figure 3.10. Thus for the Knorr model and the Das model, the coupling impedance can be set equal to the input impedance looking into the ideal transformer as $Z = Z_{in}$.

Figure 3.12 can be further simplified as shown in Figure 3.13 where $Z_{in,slot}$ is

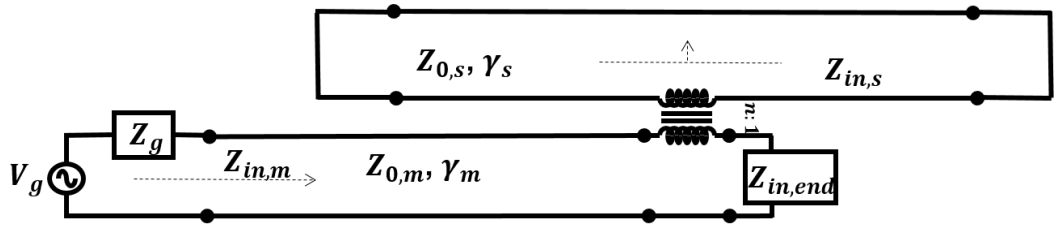

Figure 3.10: System equivalent circuit for a microstrip line coupled to a finite slot where the coupling is represented with ideal transformer.

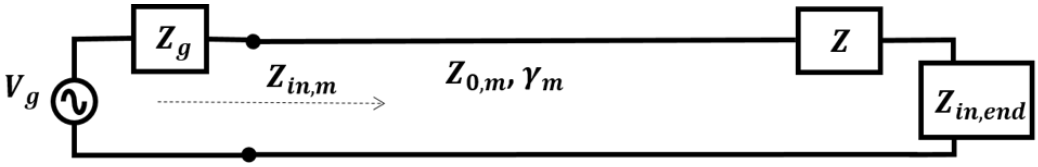

Figure 3.11: System Equivalent Circuit for a microstrip line coupled to a finite slot with coupling impedance, Z, to represent the coupling.

defined in [1] to be the parallel combination of the impedance looking to the left of the slot and the impedance looking to the right of the slot (in this case along the $\hat{x}$ direction). From Figure 3.13, it can be said that

$$Z = Z_{in} = \frac{V_{in}}{I_{in}} = \frac{V_{slot}/n}{-I_{slot}n} = \frac{Z_{in,slot}}{n^2}. \tag{3.16}$$

Now that the above study has set a framework for evaluating the models of Knorr and Das in terms of the coupling impedance Z, it is useful to determine how the turns ratio relates to General Coupling Theory and by extension to Lorentz Reciprocity Theorem. To start this discussion, the following bold statement will be explained: the turns ratio and the coupling coefficient are different quantities. If

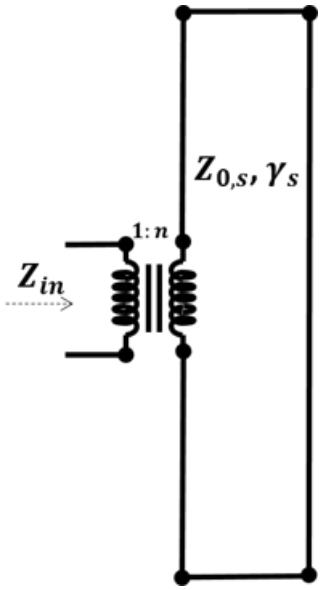

Figure 3.12: Model of the coupled finite slot from Figure 3.10 with input impedance, Z_{in}.

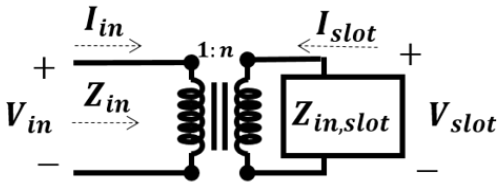

Figure 3.13: Simplified model of the coupled slot from Figure 3.12 such that the slot is represented by the slot input impedance, $Z_{in,slot}$.

two field configurations are considered, L_m is defined as the inductance due to the microstrip is defined as

$$L_m = \frac{\iint_{microstrip} B_{microstrip}}{I_{microstrip}} \tag{3.17}$$

in [24] where $I_{microstrip}$ is the current produced by the microstrip field configuration that flows along the direction of the microstrip inductance. L_s is the inductance of

the slot defined as

$$L_s = \frac{\iint_{slot} B_{slot}}{I_{slot}} \tag{3.18}$$

in [24] where I_{slot} is the current produced by the slot field configuration that flows along the direction of the slot inductance. Then the coupling coefficient in the case of pure magnetic coupling is

$$k = \frac{M}{L_m L_s} \tag{3.19}$$

where M is the mutual inductance defined in [24] as the ratio of magnetic flux due to microstrip fields to the microstrip as

$$M = \frac{\iint_{slot} B_{microstrip}}{I_{microstrip}}. \tag{3.20}$$

The magnetic field integral for the mutual inductance is taken across the width of the microstrip and over the height of the slot conductor. The magnetic field integral for the inductance due to the microstrip is taken across the width of the microstrip and over the thickness of the substrate. The turns ratio is defined in [16] as

$$n = \frac{V_{in}}{V_{out}} = \sqrt{\frac{L_m}{L_s}}. \tag{3.21}$$

Using these definitions, the turns ratio is described in terms of the coupling coefficient as

$$n = \frac{kL_m}{M}. \tag{3.22}$$

This means that for the ideal tranformer equivalent circuit shown in Figure 3.10, the coupling coefficient would be equal to

$$k = \sqrt{\frac{Z_{in,slot}}{Z}} \frac{\iint_{slot} B_{microstrip}}{\iint_{microstrip} B_{microstrip}}. \tag{3.23}$$

The ideal transformer model does not take into account electric coupling. In the microstrip-to-slot transition coupling occurs due to both magnetic coupling effects and electric coupling effects. Thus, the modified equivalent circuit given in the following section is proposed to replace the ideal transformer model supposed by the authors of the previous work described in Chapter 2.

3.4 Modified Equivalent Circuit and Circuit Analysis

In this section an improved equivalent circuit will be proposed that takes into account both electric and magnetic coupling.

The ideal transformer equivalent circuit given in the previous section can be improved by replacing the ideal transformer with a parallel LC resonant circuit as in Figure 3.14. The capacitance and the inductances are mutual capacitance and inductance values that can be calculated directly from the analytical field models that have been described for the slot in the ground plane and the microstrip feed line. In chapter 2, a link was found between Lorentz Reciprocity Theory and General Coupling Theory. It was found that a definition of mutual inductance and mutual capacitance using coupled energy is not easily achieved because of an ambiguity in the definition of the voltage difference across the mutual capacitance and in the current running through the mutual inductance. Similar to general coupling theory, the description of coupling in this section continues to use the concept of stored

energy in order to calculate the mutual inductance and mutual capacitance shown in Figure 3.14 though the concept of coupled energy will not be used directly. In

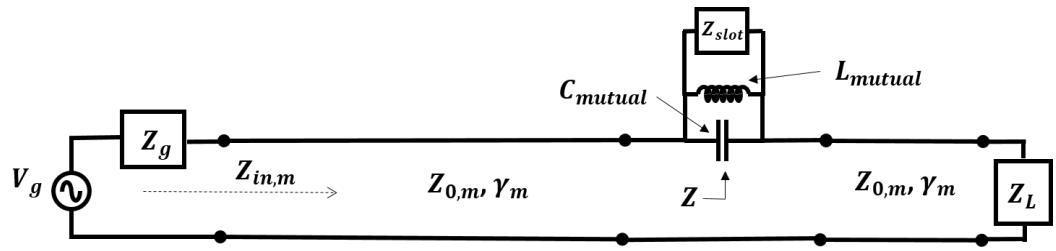

Figure 3.14: Mutual capacitance and inductance placed in system equivalent circuit that represents a microstrip coupled through a dielectric material to a finite slot in the ground plane.

order to generate the equivalent circuit shown in Figure 3.14, the fields of the slot and the microstrip were considered to have an orientation defined by the models that were introduced in Section 3.1 and 3.2. Figure 3.15 depicts an electric field wave travelling in the $\hat{y}$ direction which has only a $\hat{z}$ component. Figure 3.15 does not show the slanted field near the transition region that was described in Section 3.1, but the $\hat{z}$ directed electric field behavior near the slot transition region is assumed to slant towards conductor edges when a slot is present in the ground plane. Figure 3.15 also depicts fringing behavior at the open end of the microstrip line. Figure 3.16 shows the orientation of the electric field from a perpendicular cut with respect to the perspective of Figure 3.15. Figure 3.17 shows the orientation of the slot electric field for the first mode. The curved fringing fields that exist in the air and in the dielectric material due to the slot electric field pattern are not depicted.

Taking note of the field models presented in Section 3.1 and 3.2, the field components that exist in transition region below the slot due to the microstrip model are the E_z and H_x components. The field components that exist due to the slot field model are the E_y and H_x fields as well as E_z, E_x, H_x, and H_z which are derived from the fringing field model.

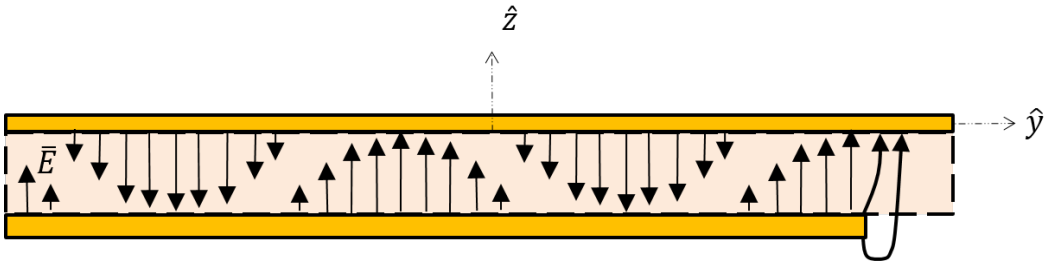

Figure 3.15: Depiction of a typical microstrip electric field orientation along length of the microstrip line, assuming a quasi-TEM field model and a model for the fringing fields at the open end of the microstrip line.

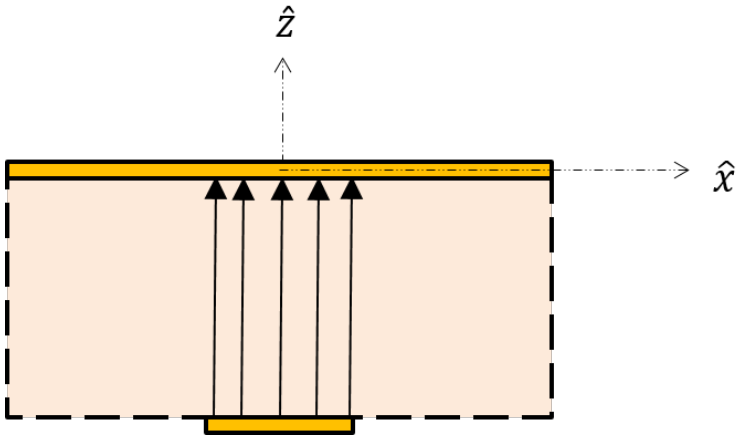

Figure 3.16: Microstrip electric field orientation based on the quasi-TEM field model as seen from the front cut of the microstrip line.

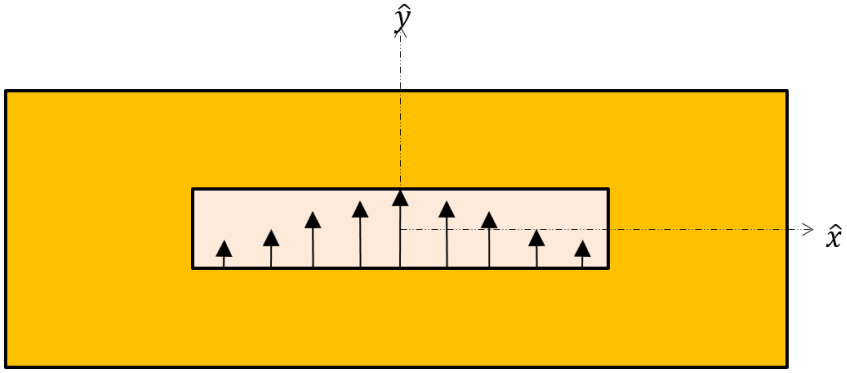

Figure 3.17: Slot electric field for the first mode.

There is an E_z component due to the microstrip fields and due to the slot fields in the transition region. Thus, moving towards an equivalent circuit model of the

transition, a parallel combination of coupled capacitance values can be defined as shown in Figure 3.18 where C_m is the capacitance produced as a result of the microstrip E_z field and C_s is the capacitance produced as a result of the slot E_z field. Figure 3.18 can be interpreted to be linked by a mutual capacitance as shown in Figure 3.19 [16]. Similarly, there is an H_x component due to the microstrip fields

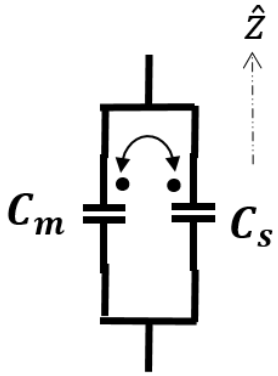

Figure 3.18: Coupled microstrip and slot capacitance representation.

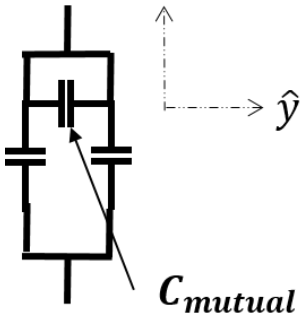

Figure 3.19: Equivalent circuit of structure shown in Figure 3.18.

and due to the slot fields. Then a parallel combination of coupled inductance values can be defined as shown in Figure 3.20. L_m is the inductance produced as a result of the microstrip H_x field and L_s is the inductance produced as a result of the slot H_x field. Figure 3.20 can be interpreted to be linked by a mutual inductance as shown in Figure 3.21 [16].

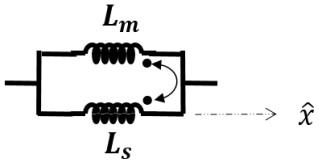

Figure 3.20: Coupled microstrip and slot inductance representation.

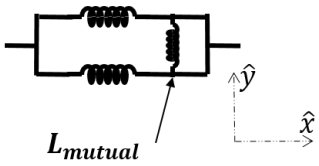

Figure 3.21: Equivalent circuit corresponding to Figure 3.20.

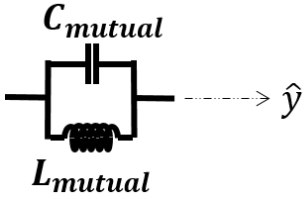

Figure 3.22: Mutual capacitance and inductance in parallel to be used in the system equivalent circuit.

Because of the shared field directions in the transition region between the microstrip conductor and the finite slot, self impedance values have been defined for the purpose of obtaining coupling impedance values to represent electric coupling and magnetic coupling behavior at the transition region. Then because the coupled impedances exist in the same location on the structure, the voltage difference across them is the same. Thus, the mutual capacitance and mutual inductance values can be placed in parallel as shown in Figure 3.22. The circuit shown in Figure 3.22 can then be implemented in a transmission line equivalent circuit for the system. This equivalent circuit is shown in Figure 3.14 where Z_{slot} is the input impedance looking into the aperture.

In order to calculate the coupling impedance, Z, shown in Figure 3.14, it must

first be assumed that the permeability in the dielectric is $\mu = \mu_0\mu_r$, and the permittivity is $\epsilon = \epsilon_0\epsilon_r$. It is assumed that Z_{slot} which is the input impedance of the slot is found using Cohn's method given in [15] and that $E_{y,slot}$ is the $\hat{y}$ directed field found using Ruyle's method given in [1]. A relationship between mutual impedance and the coupled impedances that cause the mutual impedance is outlined in [16]. For the purpose of this research, it allows for the calculation of the mutual impedance using either the slot inductance and slot capacitance or the microstrip inductance and microstrip capacitance. In addition to these, some current and voltage relationships are required. Because the slot field model takes into account more modes than the microstrip field model does, the slot capacitance and slot inductance are chosen in the calculation of the mutual impedance effects.

The concept of stored energy from Chapter 2 is used to related the stored energy due to the slot fields to an equivalent slot capacitance by

$$C_s = \frac{\epsilon \iiint_V |E_{y,slot}|^2 + |E_{z,slot}|^2 + |E_{x,slot}|^2 dxdydz}{|V_{z,m}|^2} \tag{3.24}$$

where $V_{z,m}$ is the microstrip voltage at the first edge of the slot across the dielectric in the $\hat{z}$ direction. The microstrip voltage is used here with the thought that the microstrip carries energy to the slot. Then the impedance of the slot capacitance defined in Equation 3.24 can be found as

$$Z_{c,s} = \frac{1}{j\omega C_s}. \tag{3.25}$$

Because no conductor exists in the transition region, the concept of displacement current is used to determine the $\hat{z}$ directed current due to the slot fields in the di-

electric material as

$$I_{z,s} = j\omega\epsilon \iint_S E_{z,slot} dxdy \tag{3.26}$$

where the electric field is integrated over the surface extending along the width of the microstrip line and the length of the width of the slot line. Then the vector normal to this surface is $\hat{z}$ directed.

Using the quasi-TEM Microstrip approximation, the current due to the microstrip fields can be defined as

$$I_{z,m} = \frac{V_0}{Z_0}(e^{-\gamma_m y} - \Gamma_0 e^{\gamma_m y}) \tag{3.27}$$

as shown in Section 3.1.

The purely imaginary mutual impedance due to the mutual capacitance term $C_m = \dfrac{1}{j\omega C_m}$ can be found using the relation

$$Z_{c,mutual} = \frac{V_z - Z_{cs} I_{z,s}}{I_{z,m}} \tag{3.28}$$

which is based on a definition in [16].

The voltage found using the slot fields across the width of the mirostrip conductor within the dielectric is found to be

$$V_{x,s} = E_{s,x} w_m. \tag{3.29}$$

Using the concept of displacement current again, the $\hat{x}$ directed current can be found

as

$$I_{x,s} = j\omega\epsilon \iint_S E_{x,slot} dydz. \tag{3.30}$$

where the surface S extends across the width of the slot and the height of the dielectric such that the vector normal to the surface is $\hat{x}$ directed. The slot inductance is defined in terms of the total stored magnetic energy as

$$L_s = 4\frac{\mu_0\mu_r \iiint_V |H_{x,slot}|^2 + |H_{z,slot}|^2 dxdydz}{|I_{x,s}|^2} \tag{3.31}$$

where $I_{x,s}$ is the current flowing though the slot inductance as defined in Equation 3.30.

The impedance due to the slot inductance can then be defined as

$$Z_{l,s} = j\omega L_s. \tag{3.32}$$

$I_{x,m}$ is the current through the microstrip inductance. It is found by taking the integral along the slot width in a line of $H_{m,x}$ according to

$$I_{x,m} = -\int_l J_{x,m} dl \tag{3.33}$$

where

$$\bar{J_{x,m}} = \bar{H_m} \cdot \hat{n} = H_{m,z} + H_{m,y}. \tag{3.34}$$

Then,

$$I_{x,m} = -\int_x (H_{m,z} + H_{m,y})dx. \tag{3.35}$$

Since $H_{m,z}$ and $H_{m,y}$ do not exist in the quasi-TEM microstrip model, $I_{x,m}$ is assumed to be proportional to the line integral across the width of the microstrip of the $\hat{x}$ directed microstrip magnetic field. Future research will require developing a field model for the fringing effects along the length of the microstrip which exist primarily outside of the transition region considered in this thesis.

Finally, the mutual impedance due to the $\hat{x}$ directed magnetic fields of the slot and the microstrip can be found using a relation from [16] as

$$Z_{l,mutual} = \frac{V_x - Z_{l,s}I_{x,s}}{I_{x,m}}. \tag{3.36}$$

3.5 Conclusions about Methodology

This chapter served to introduce the field models used to develop an improved coupling model as well as discussing the equivalent circuits of previous models that depend on an ideal transformer representation. The proposed coupling model is different from the models outlined in Chapter 2 that depend on Lorentz Reciprocity, but it still accounts for electric and magnetic coupling effects using the concept of stored energy and depends on the idea that aligning field components contribute to coupling. This model will be tested in the following chapter and will be compared to measured and simulated results as well as results generated using the work of Knorr and Das.

Chapter 4

Measured Results

This chapter presents simulated and measured results to compare to the proposed coupling model. The model is tested against HFSS simulated results using the coupling impedance metric, Z. The model is tested against measured results using a de-embedded system input impedance metric, $Z_{in,d}$. It will be seen that the proposed model may be more accurate in some cases than the models proposed by Das in [6] and Knorr in [5]. The model proposed by Pozar in [7] will not be analyzed due to the complexity of the Green's function field model he proposes.

4.1 HFSS (FEM) Analysis

In order to verify that the coupling model works, it is useful to compare the analytical results to simulated results. In order to do this, two simulation files were built in the High Frequency Electromagnetic Field Simulation Software (HFSS), which is a software based on Finite Element Method. The first is a microstrip-fed slot structure as shown in Figure 4.1. Figure 4.1 shows the side of the microstrip-fed slot structure that includes the microstrip conductor. On the opposite side of the dielectric is the ground plane that contains the half wavelength slot. This structure was designed such that the microstrip extends a quarter wavelength past the center

of the slot along a direction orthogonal to the length of the slot. The second simulation was run on a structure the same as the one shown in Figure 4.1 except with a filled-in ground plane instead of a slot existing in the ground plane.

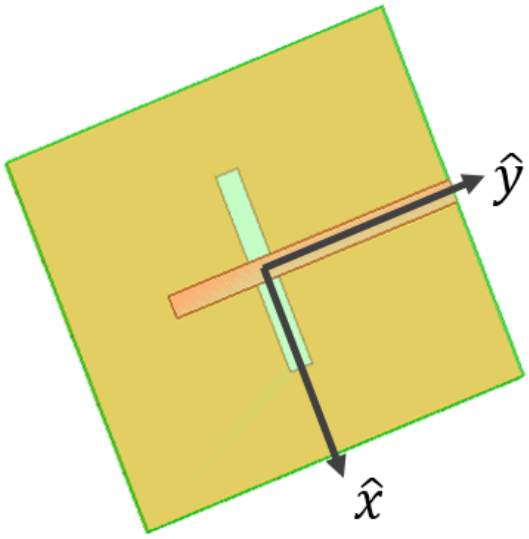

Figure 4.1: Microstrip-fed Slot Antenna (bottom view).

The equivalent circuit of the microstrip-fed slot structure is shown in Figure 4.2 where V_g is the generator voltage, Z_g is the generator impedance, $Z_{0,m}$ is the characteristic impedance of the microstrip feed line, Z is the coupling impedance representing the aperture discontinuity, and $Z_{in,end}$ is the input impedance looking in to the quarter wavelength of line (adapted for some design frequency) that extends past the slot. This structure can be separated into two-port network sections as shown in Figure 4.3. The microstrip-line two-port network and the coupling impedance two-port network can both be described by ABCD matrices [4]. Because they are in series, a total ABCD matrix to describe the cascaded sections can be as

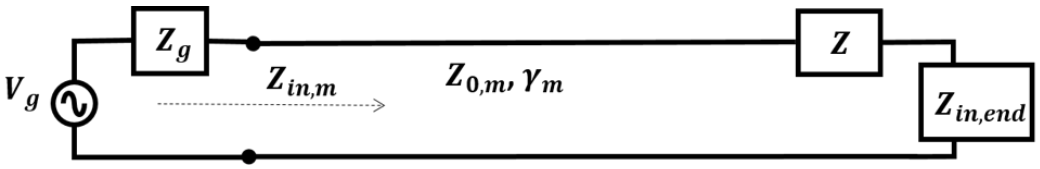

Figure 4.2: Microstrip-fed slot equivalent circuit.

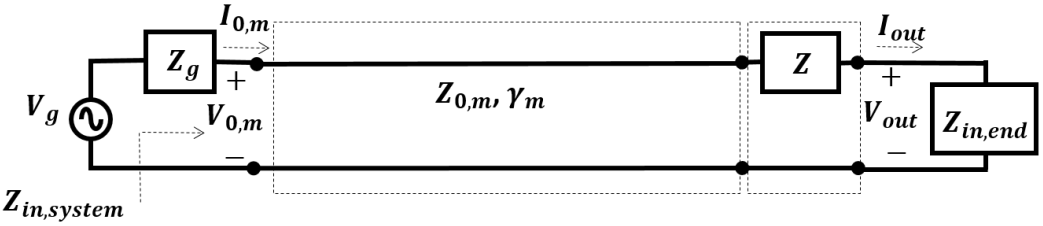

Figure 4.3: Equivalent Circuit with series coupling impedance depicting two-port sections.

$$\begin{bmatrix} A_{total} & B_{total} \\ C_{total} & D_{total} \end{bmatrix} = \begin{bmatrix} cosh(\gamma_m l_m) & Z_{0,m} sinh(\gamma_m l_m) \\ Y_{0,m} sinh(\gamma_m l_m) & cosh(\gamma_m l_m) \end{bmatrix} \begin{bmatrix} 1 & Z \\ 0 & 1 \end{bmatrix} \quad (4.1)$$

where Z is the unknown coupling impedance that will be solved for, $\gamma_m = \alpha_m + j\beta_m$ represents the attenuation and propagation constant of the microstrip line, $Z_{0,m}$ is the characteristic impedance of the microstrip line, $Y_{0,m} = \dfrac{1}{Z_{0,m}}$, and l_m is the length of the microstrip between the feed and the center of the slot (not including the length of line extending past the center of the slot). $V_{0,m}$, $I_{0,m}$, V_{out}, and I_{out} as shown in Figure 4.3 are related to the total ABCD matrix as

$$\begin{bmatrix} V_{0,m} \\ I_{0,m} \end{bmatrix} = \begin{bmatrix} A_{total} & B_{total} \\ C_{total} & D_{total} \end{bmatrix} \begin{bmatrix} V_{out} \\ I_{out} \end{bmatrix}. \quad (4.2)$$

The input impedance of the system can be related to the total ABCD matrix by

$$Z_{in,system} = \frac{A_{total}Z_{in,end} + B_{total}}{C_{total}Z_{in,end} + D_{total}}. \tag{4.3}$$

The system input impedance, $Z_{in,system}$ can be pulled from the microstrip-to-slot HFSS simulation. Then γ_m, $Z_{0,m}$, and $Z_{in,end}$ can be pulled from the microstrip HFSS simulation. The coupling impedance can be described in terms of these as

$$Z = -\frac{Z_{in,end}cosh(\gamma_m l_m) - Y_{0,m}Z_{in,system}sinh(\gamma_m l_m) + Z_{0,m}sinh(\gamma_m l_m)}{cosh(\gamma_m l_m) - Y_{0,m}sinh(\gamma_m l_m)}. \tag{4.4}$$

The following section will detail results of this analysis compared to the analytical results.

4.2 Results

This chapter presents simulated and measured results to compare to the proposed coupling model. The model is tested against HFSS simulated results using the coupling impedance metric, Z. The model is tested against measured results using a de-embedded system input impedance metric, $Z_{in,d}$. It will be seen that the proposed model may be more accurate in some cases than the models proposed by Das in [6] and Knorr in [5]. The model proposed by Pozar in [7] will not be analyzed due to the complexity of the Green's function field model he proposes.

4.2.1 Coupling Impedance Simulation Results

This section will analyze two test cases to show the difference between the analytical results generated using the model proposed in Section 3.4 and the results

Test Case	ϵ_r	w_m (mm)	w_s (mm)	d
1	10.2	1.1	1.2	1.2
2	2.2	5	0.7	1.6

Table 4.1: Simulated Antenna Parameters

obtained by extracting the coupled system input impedance, the microstrip propagation constant, attenuation constant, port impedance, and microstrip load impedance from HFSS as outlined in Section 4.1. The metric that will be used to compare the measured results to the simulated results is the coupling impedance Z.

The parameters of the test cases that will be considered in this section are given in Table 4.1. Some important comparisons to show how the analytical microstrip field model compares to the fields produced in HFSS are given. To this end, the microstrip characteristic impedance $Z_{0,m}$, the propagation constant $\gamma_m = \alpha + j\beta$, and the load impedance, $Z_{l,m}$, that represents the fringing effects at the open end of the microstrip line are compared between the analytical model and the values extracted from HFSS. Beyond this, results are compared for the analytical coupling impedance that results when the equivalent circuit model of Chapter 3.4 is applied to the analytical slot field models that were also introduced in Chapter 3.

First Test Case

In order to develop an analytical solution for the first test case, the pertinent analytical field modal parameters for the microstrip line have been compared to those extracted from HFSS. For the first test case, γ_m is shown in Figure 4.4, $Z_{0,m}$ is shown in Figure 4.5, and $Z_{l,m}$ is shown in Figure 4.6. It can be seen that the HFSS microstrip parameters of γ_m, $Z_{0,m}$, and $Z_{l,m}$ match the analytical microstrip parameters fairly well. Because of the alignment between these parameters, confidence can be placed in the quasi-TEM microstrip field model.

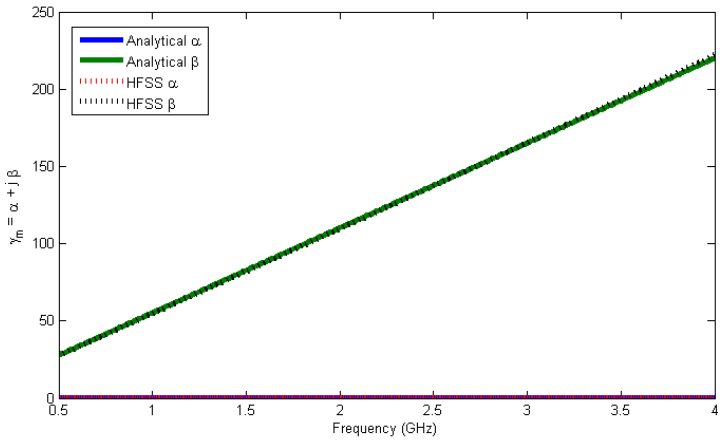

Figure 4.4: Microstrip γ_m for $\epsilon_r = 10.2$, $d = 1.2$ mm, $w_s = 1.2$ mm, $w_m = 1.1$ mm, and $l_s = 19.1$ mm.

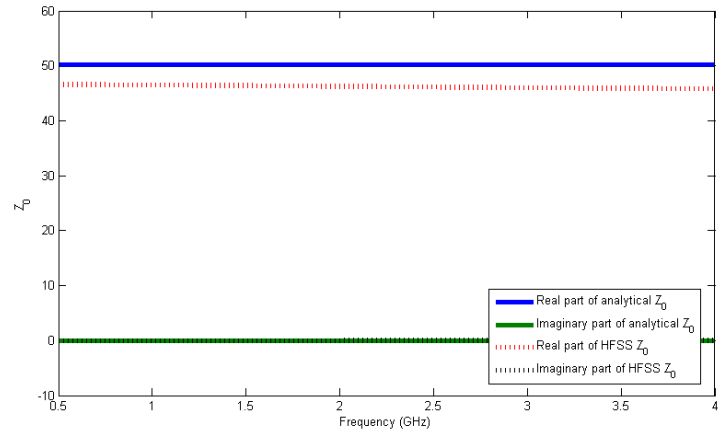

Figure 4.5: Microstrip characteristic impedance, $Z_{0,m}$, for $\epsilon_r = 10.2$, $d = 1.2$ mm, $w_s = 1.2$ mm, $w_m = 1.1$ mm, and $l_s = 19.1$ mm.

Plots comparing the analytical model to the HFSS simulation and to the Das and Knorr models are shown in Figures 4.7 and 4.8. The analytical model for the case where the fringing fields due to the slot field model are assumed to be constant along the width of the microstrip inside the conductor is compared to the case where multiple fringing fields are taken into account by basing their calculation on the magnitude of the dominant field in the slot. From these results, it appears that

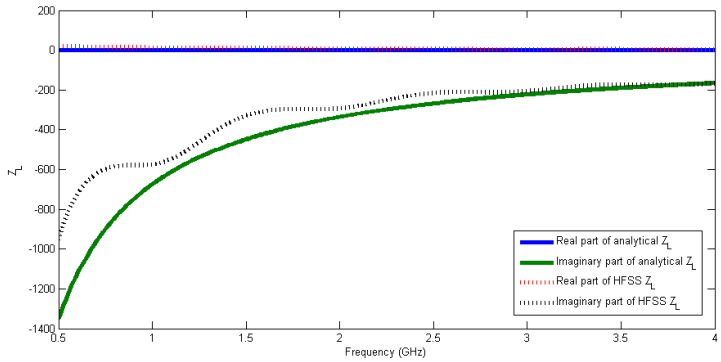

Figure 4.6: Microstrip fringing load impedance, $Z_{l,m}$, for $\epsilon_r = 10.2$, $d = 1.2$ mm, $w_s = 1.2$ mm, $w_m = 1.1$ mm, and $l_s = 19.1$ mm.

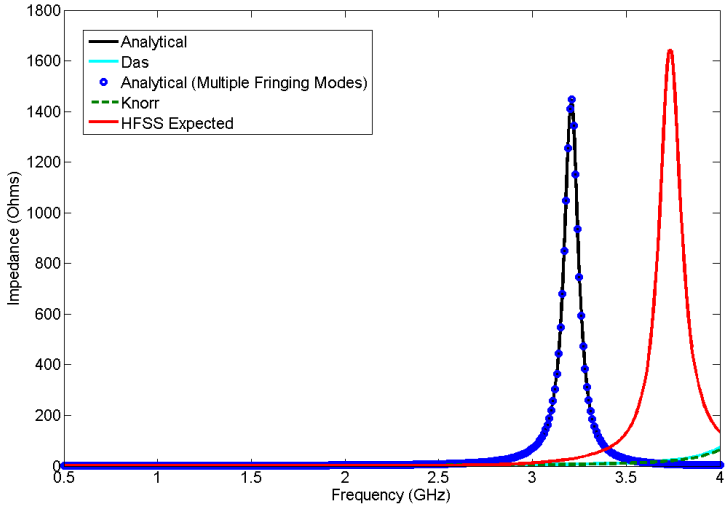

Figure 4.7: Real part of the analytical coupling impedance, $Re(Z)$, assuming constant fringing fields plotted against the analytical coupling impedance result taking into account multiple modes in the fringing fields, the Knorr model coupling impedance result, the Das model coupling impedance result, and the HFSS expected coupling impedance result for $\epsilon_r = 10.2$, $d = 1.2$ mm, $w_s = 1.2$ mm, $w_m = 1.1$ mm, and $l_s = 19.1$ mm.

for this test case the coupling impedance calculated using the improved model can predict the actual system coupling behavior more accurately than either the Knorr model or the Das model. The Knorr model and the Das model align well with each other, but they are shifted up in frequency from the HFSS expected result. The

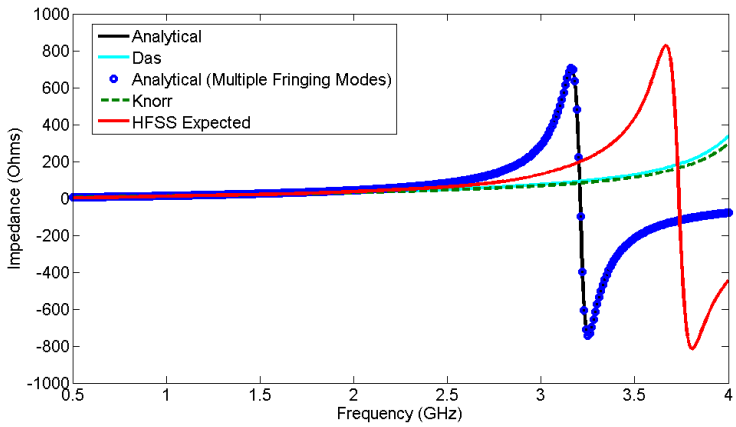

Figure 4.8: Imaginary part of the analytical coupling impedance, $Im(Z)$, assuming constant fringing fields plotted against the analytical coupling impedance result taking into account multiple modes in the fringing fields, the Knorr model coupling impedance result, the Das model coupling impedance result, and the HFSS expected coupling impedance result for $\epsilon_r = 10.2$, $d = 1.2$ mm, $w_s = 1.2$ mm, $w_m = 1.1$ mm, and $l_s = 19.1$ mm.

proposed model has a Z that is shifted down some in frequency from the HFSS expected Z. Additionally for this test case, taking into account multiple modes in the slot fringing fields does not appear to have an effect on the predicted coupling impedance.

4.2.2 Second Test Case

For the second test case, analytical parameters are again compared to those pulled from HFSS where γ_m is shown in Figure 4.9, $Z_{0,m}$ is shown in Figure 4.10, and $Z_{l,m}$ is shown in Figure 4.11.

As in the previous section, the analytical microstrip field model aligns will with HFSS.

Next, plots comparing the analytical model to the HFSS simulation and to the Das and Knorr models are shown in Figures 4.7 and 4.8. Again, the analytical

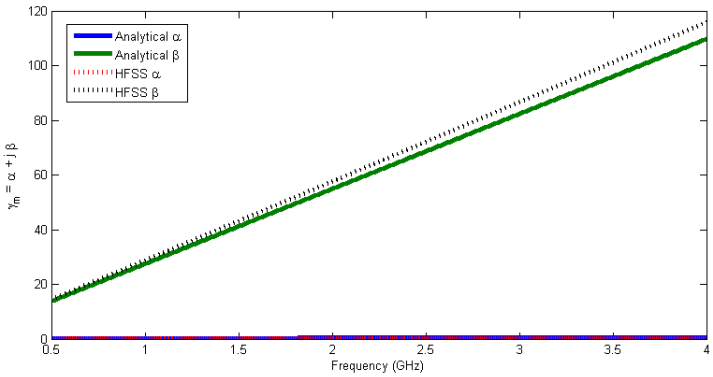

Figure 4.9: Microstrip γ_m for $\epsilon_r = 2.2$, $d = 1.6$ mm, $w_s = 0.7$ mm, $w_m = 5.0$ mm, and $l_s = 40.2$ mm.

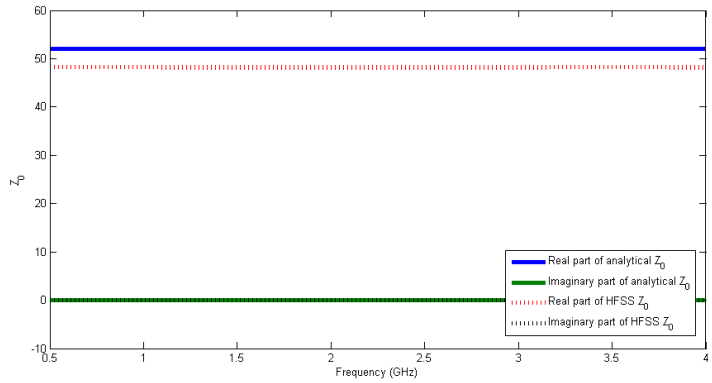

Figure 4.10: Microstrip characteristic impedance, $Z_{0,m}$, for $\epsilon_r = 2.2$, $d = 1.6$ mm, $w_s = 0.7$ mm, $w_m = 5.0$ mm, and $l_s = 40.2$ mm.

model assuming constant slot fringing fields is plotted against the analytical model that takes into account multiple modes in the slot fringing fields.

From these results, it appears that for the second test case the coupling impedance calculated using the improved model can predict the actual system coupling behavior as accurately as either the Knorr model or the Das model if multiple slot fringing modes are taken into account. If these multiple fringing fields are assumed to be constant, then extra resonances become pronounced in the coupling impedance.

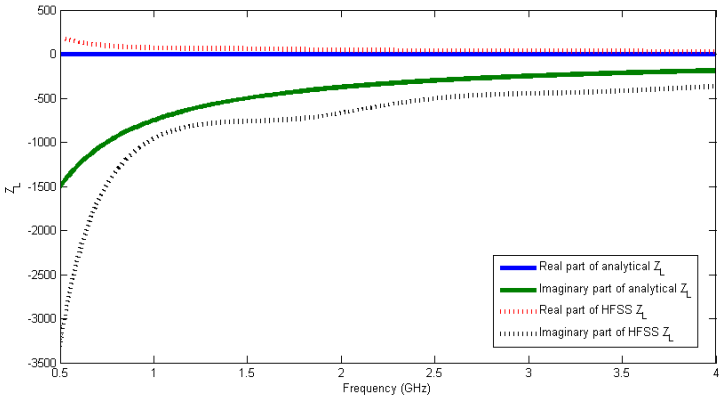

Figure 4.11: Microstrip fringing load impedance, $Z_{l,m}$, for $\epsilon_r = 2.2$, $d = 1.6$ mm, $w_s = 0.7$ mm, $w_m = 5.0$ mm, and $l_s = 40.2$ mm.

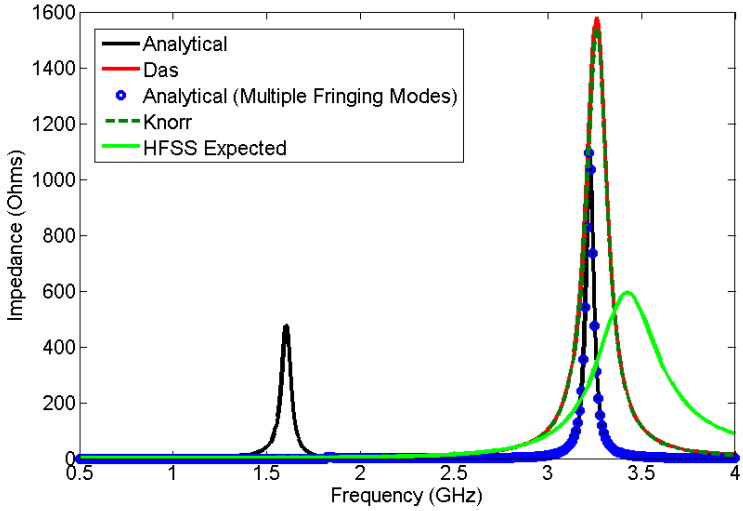

Figure 4.12: Real part of the analytical coupling impedance, $Re(Z)$, assuming constant fringing fields plotted against the analytical coupling impedance result taking into account multiple modes in the fringing fields, the Knorr model coupling impedance result, the Das model coupling impedance result, and the HFSS expected coupling impedance result for $\epsilon_r = 2.2$, $d = 1.6$ mm, $w_s = 0.7$ mm, $w_m = 5.0$ mm, and $l_s = 40.2$ mm.

Fringing Fields

Fringing fields exist at the slot edges. This may cause some added reactive effects to the input impedance. The fringing fields could be defined as shunt capacitances,

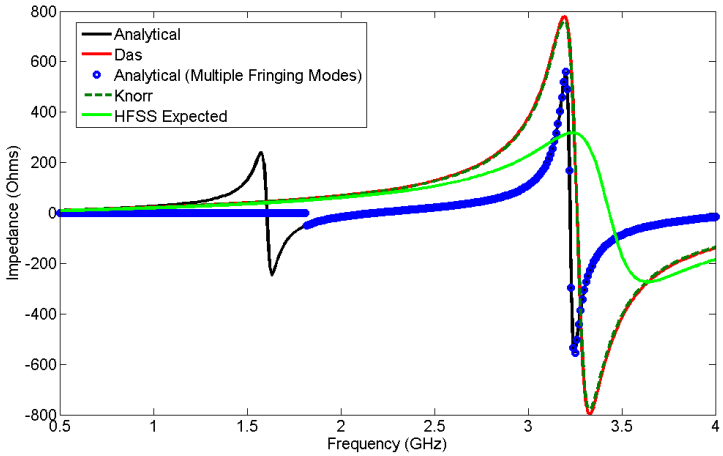

Figure 4.13: Imaginary part of the analytical coupling impedance, $Im(Z)$, assuming constant fringing fields plotted against the analytical coupling impedance result taking into account multiple modes in the fringing fields, the Knorr model coupling impedance result, the Das model coupling impedance result, and the HFSS expected coupling impedance result for $\epsilon_r = 2.2$, $d = 1.6$ mm, $w_s = 0.7$ mm, $w_m = 5.0$ mm, $l_s = 40.2$ mm

C_{f1} and C_{f2}, as shown in Figure 4.14. In the model proposed by this thesis, fringing effects at the slot edges have been taken into account, in part, using a modified effective wavelength and by perturbing the electric field lines to reach towards the slot edges. Future work may include better modelling the fringing effects at the edges

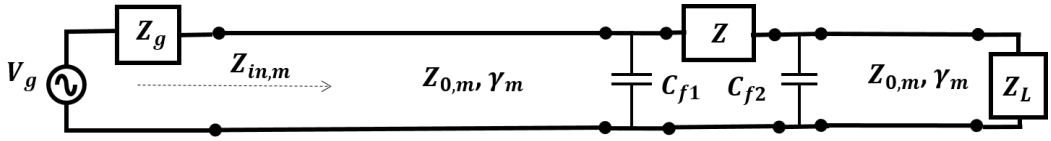

Figure 4.14: Equivalent circuit with fringing capacitance to take into account fringing effects at the slot edges.

of the slot. To do this, analysis of the electric field behavior inside the dielectric material would need to be approximated. Capacitance is defined as

$$C_{t1} = C_{t2} = \frac{Q}{\triangle V} \tag{4.5}$$

where Q is

$$Q = \oiint_S q_{es} \cdot d\bar{S} \tag{4.6}$$

and $q_{es} = \hat{n} \cdot (\bar{D_1} - \bar{D_2}) = \hat{z}\bar{D_1}$. $\bar{D_1} = \epsilon\bar{E_1}$ is the field in the substrate, $D_2 = \epsilon E_2 = 0$ is the field in the conductor, and $\bar{q_{es}}$ is the surface charge density. The charges of interest are the charge differences in the $\hat{z}$ direction on either edge of the slot width on the microstrip. The voltage $\triangle V$ is might be found by integrating the electric field along the $\hat{z}$ direction on either edge of the slot width. This observation is motivation for future work and is not explored further in this thesis.

4.2.3 Coupling Impedance Measured Results

In order to test the model for coupling that was proposed in Chapter 3 against measured results, three antennas were fabricated. Table 4.2 gives the design parameters for each antenna and Figure 4.15 shows the feed line side and the ground plane side of each antenna where the finite slot is present. All three antennas were fabricated using material having 0.0175 mm of copper cladding on top and bottom. Additionally, each antenna was built such that the center of the finite slot was placed in the center of a 100 mm by 100 mm ground plane. It is impractical to measure the

Antenna	ϵ_r	w_m (mm)	d (mm)	l_s	w_s
A	3.00	0.6753	0.25	42.397	0.7
B	6.15	0.3681	0.25	31.711	1.2
C	10.2	0.6004	0.64	25.337	1.2

Table 4.2: Measured antenna parameters

coupling impedance, Z, for these antennas because they are designed to have only one port. Thus, measured results in this section will be given in the form of the in-

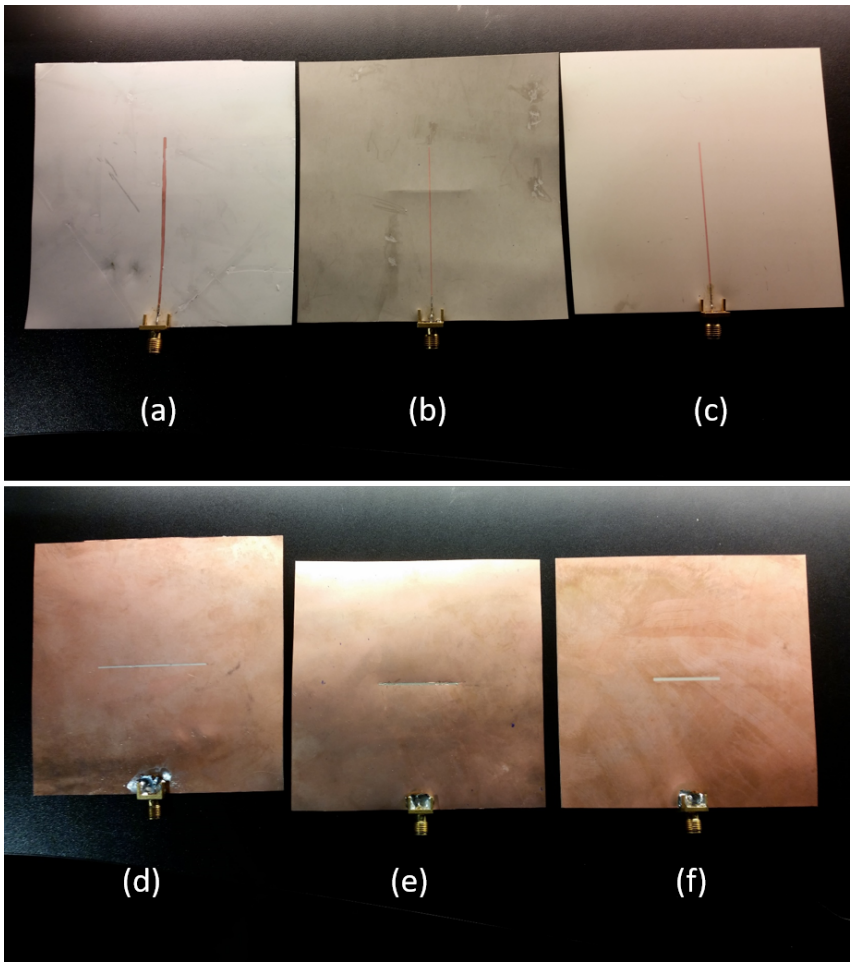

Figure 4.15: Measured slot antennas corresponding to Table 4.2 such that is shows the (a) feedline side of antenna A, (b) feedline side of antenna B, (c) feedline side of antenna C, (d) ground plane side of antenna A, (e) ground plane side of antenna B, and (f) ground plane side of antenna C.

put impedance at the feed port of the antenna de-embedded to the transition region (in the center of the slot). To obtain the measured results, the one-port scattering parameters were pulled from a calibrated Agilent N5225A Network Analyzer. The

S_{11} parameter was used to find the de-embedded input impedance, $Z_{in,d}$ using

$$\begin{aligned}
\beta_m &= \frac{2\pi}{\lambda_{eff,m}} = \frac{2\pi f\sqrt{\epsilon_{eff,m}}}{c} \\
\beta_c &= \frac{2\pi}{\lambda_{eff,c}} = \frac{2\pi f\sqrt{\epsilon_c}}{c} \\
S_{11,d} &= S_{11}e^{2j\beta l} = S_{11}e^{2j\beta_m l_m + 2j\beta_c l_c} \\
Z_{in,d} &= Z_{0,m}\frac{1+S_{11,de-embedded}}{1-S_{11,d}}
\end{aligned} \tag{4.7}$$

where β_m is the propagation constant of the microstrip line, $\lambda_{eff,m}$ is the effective wavelength of the wave travelling down the microstrip line, f is the frequency, $\epsilon_{eff,m}$ is the effective permittivity of the dielectric material between the microstrip conductor and the ground plane calculated using a closed form expression given in [4], c is the speed of light, $\lambda_{eff,c}$ is the effective wavelength associated with the 50 ohm coaxial connector, ϵ_c is the permittivity of the material in the connector, S_{11} is the one-port scattering parameter pulled from the network analyzer, $S_{11,d}$ is the de-embedded S_{11} to the center of the transition region, l_m is the length of line from the edge of the transition between the microstrip conductor and the coaxial connector to the center of the slot, l_c is the length of the connector, and Z_0 is the characteristic impedance of the microstrip line and the connector which are assumed to 50 ohms. For all the measured results, l_c is 5.46 mm based on a caliper measurement from the point where the connector connects to the microstrip conductor to the point where the connector reaches the calibrated network analyzer cable. Additionally, l_m is 50 mm for all of the measured results. The measured results are compared to de-embedded results pulled from HFSS as well as de-embedded analytical results for antennas A, B, and C in this section. An example of an HFSS microstrip coupled to slot structure that is de-embedded in HFSS is shown in Figure 4.16. The

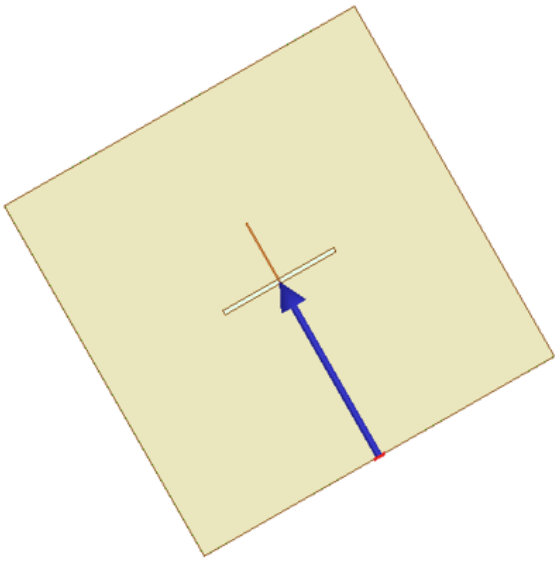

Figure 4.16: HFSS microstrip coupled to slot that is de-embedded to the center of the finite slot.

built in de-embedding approach is used to de-embed the HFSS simulated system input impedance to the center of the slot. Finally, the analytical de-embedded input impedance corresponding to the HFSS simulated and measured de-embedded input impedances is found by cascading an ABCD matrix including the analytically calculated coupling impedance, Z, found using the method proposed in Section 3.4 (assuming a constant fringing field) with an ABCD matrix representing the length of microstrip line extending past the transition region. Then the analytical de-embedded input impedance can be found using

$$Z_{in,d} = \frac{AZ_l + B}{CZ_l + d} \tag{4.8}$$

where A, B, C, and D are defined to be the matrix entries of the cascade of the ABCD matrix representing the series coupling impedance with the ABCD matrix representing the length of microstrip line extending past the center of the transition

region. This can be found according to a method given in [4] as

$$\begin{bmatrix} A & B \\ C & D \end{bmatrix} = \begin{bmatrix} 1 & Z \\ 0 & 1 \end{bmatrix} \begin{bmatrix} cosh(\gamma_m l_{m,end}) & Z_{0,m} sinh(\gamma_m l_{m,end}) \\ Y_{0,m} sinh(\gamma_m l_{m,end}) & cosh(\gamma_m l_{m,end}) \end{bmatrix} \tag{4.9}$$

where Z is the coupling impedance, $l_{m,end}$ represents the length of microstrip line extending past the center of the transition region, and $\gamma_m = \alpha_d + j\beta$ represents the attenuation due to dielectric loss and propagation constant on the microstrip line such that conductor losses are assumed to be negligible due to the high conductivity of copper [4].

Figure 4.17 compares the real part of the measured $Z_{in,d}$ against the HFSS simulated $Z_{in,d}$ and the impedance generated using the model proposed in Section 3.4 for Antenna A. Figure 4.18 shows this same comparison for the imaginary part of $Z_{in,d}$ for Antenna A. With a relative permittivity of $\epsilon_r = 3$, the results of Antenna A show fairly good agreement between analytical (model) results and HFSS results for the second resonance that appears in the HFSS simulation. The model does not seem to predict the first resonance that appears in both the measured and HFSS simulations. Some potential reasons for this will be suggested after all three antenna results have been presented.

Similar to Figure 4.17, Figure 4.19 compares the real part of the measured $Z_{in,d}$ against the HFSS simulated $Z_{in,d}$ and the impedance generated using the model proposed in Section 3.4 for Antenna B. Then similar to Figure 4.18, Figure 4.20 shows the comparison for the imaginary part of $Z_{in,d}$ for Antenna B. In this test case, the analytical model predicts two resonances over the frequencies of interest that are shifted in frequency from both the simulated and measured results. In addition to this, the predicted impedance peaks are of a larger magnitude than the

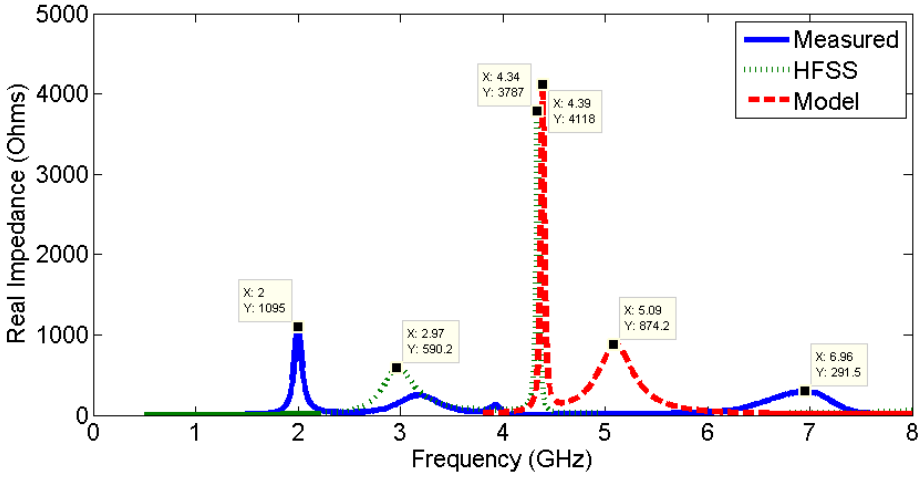

Figure 4.17: Real part of the de-embedded input impedance, $Z_{in,d}$, for antenna A.

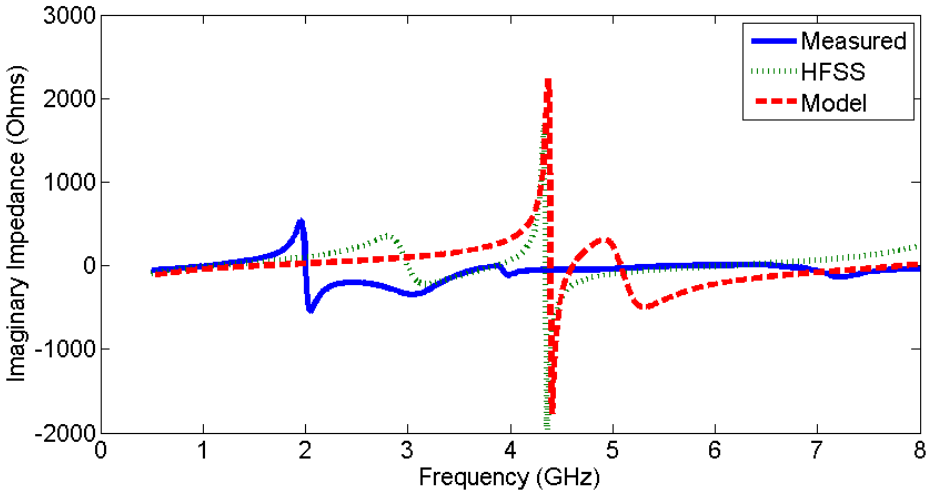

Figure 4.18: Imaginary part of the de-embedded input impedance, $Z_{in,d}$, for antenna A.

measured and simulated values.

Figure 4.21 compares the real part of the measured impedance against the HFSS impedance and the impedance generated using the model proposed in Section 3.4 for Antenna C. Figure 4.22 shows the comparison for the imaginary part of $Z_{in,d}$ for Antenna C. Similar to the stated observations for Figures 4.19 and 4.20, the analytical result for $Z_{in,d}$ does predict two resonances in the frequency range of

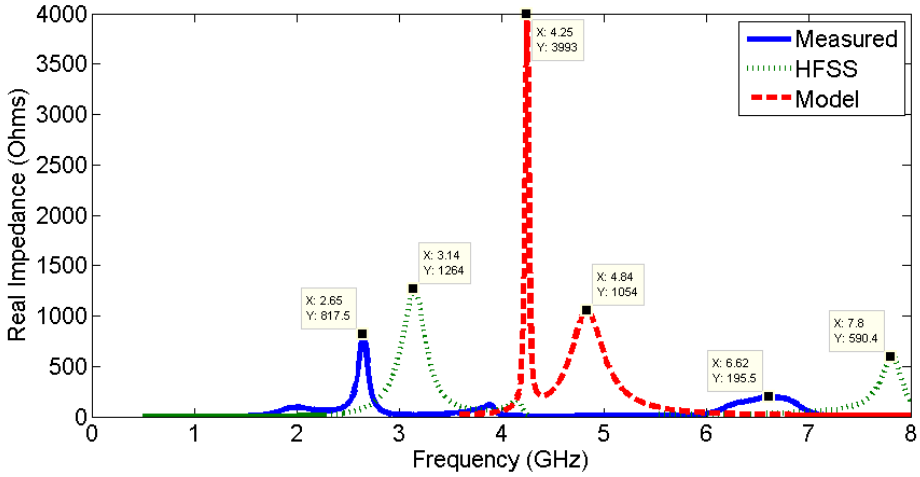

Figure 4.19: Real part of the de-embedded input impedance, $Z_{in,d}$, for antenna B.

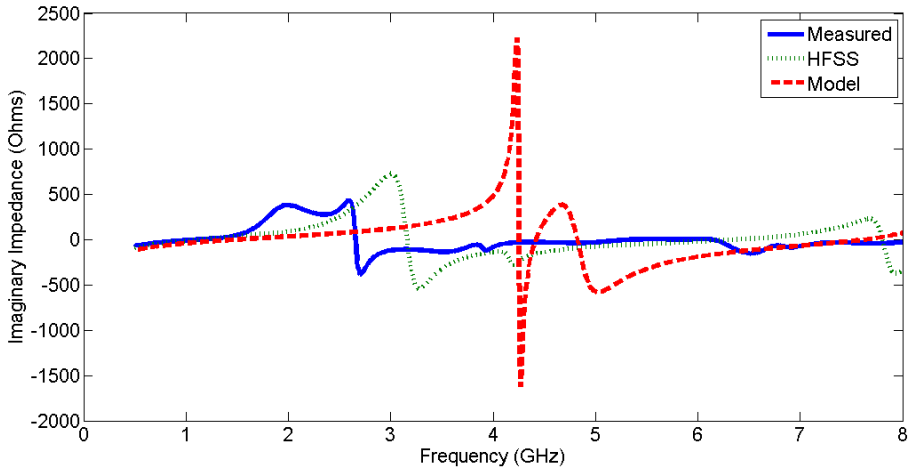

Figure 4.20: Imaginary part of the de-embedded input impedance, $Z_{in,d}$, for antenna B.

interest, but these peaks are shifted in frequency from both the measured and HFSS simulated impedance values.

An observation of the data shown in Figures 4.17 through 4.22 is that the measured and HFSS simulated results are shifted in frequency and do not align exactly. This difference may be caused because the effects of the solder used to attach the connector to the board have not been taken into account or because there may exist

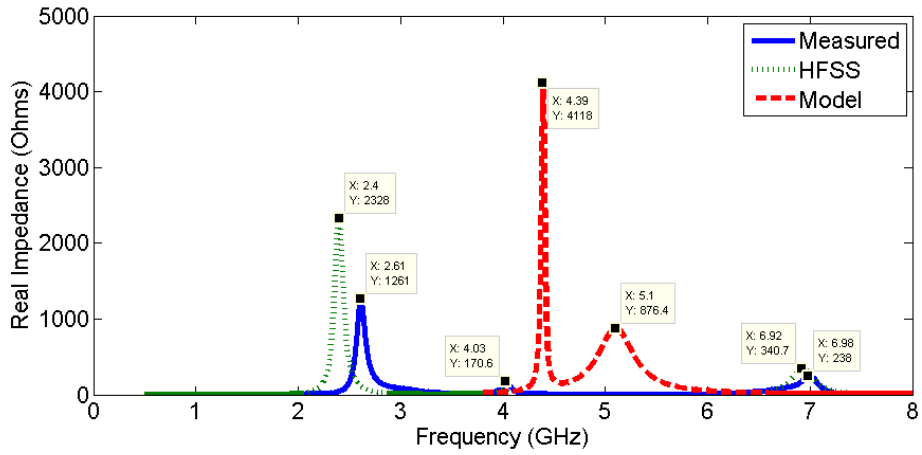

Figure 4.21: Real part of the de-embedded input impedance, $Z_{in,d}$, for antenna C.

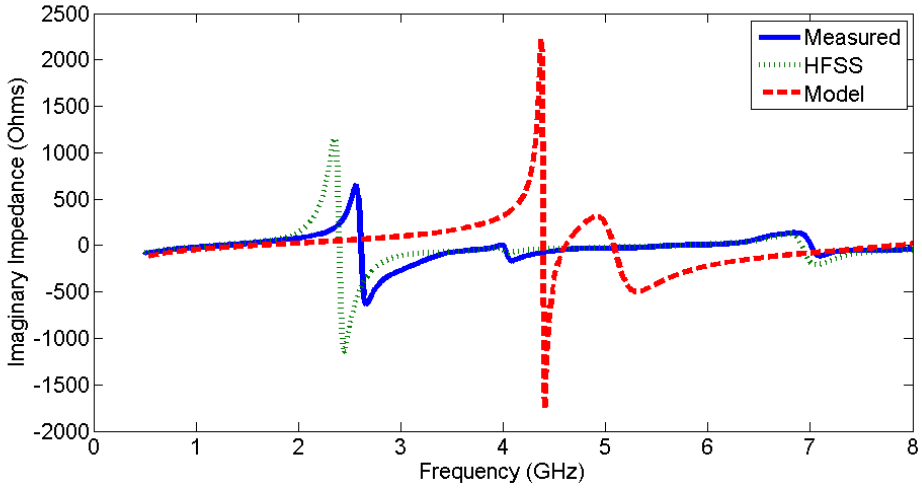

Figure 4.22: Imaginary part of the de-embedded input impedance, $Z_{in,d}$, for antenna C.

small inconsistencies in the shape of the slot caused during the lithography fabrication process. It should be noted that the HFSS simulated results align more with the measured results as the test cases increase in permittivity.

From the measured results shown in Figures 4.17 through 4.22, it can be seen that, in general, there is a large discrepancy between analytical, simulated, and measured results. In general, if the predicted system coupling impedance is not exactly

correct, extra resonances can appear on the system level. These extra resonances can change how the de-embedded analytical system impedance, $Z_{in,d}$, appears. This realization provides an argument for the need to develop a highly accurate coupling model. The work that has been done in this thesis provides a sound theoretical framework upon which a more improved model can be developed. To this end, some future work that can be done on this topic to move towards a better analytical model for the coupling between a microstrip line and a slot is given in Chapter 5.

Chapter 5

Conclusions and Future Research

A model has been proposed in Section 3.4 to describe the specific case of coupling between a microstrip feed line and a finite slot in a ground plane that rivals the accuracy of the previous proposed models in [5] and [6]. This model depends on defining a mutual inductance and mutual capacitance based on analytical field models for the microstrip line and for the slot line, which is a new perspective on the coupling problem. This method is flexible such that it could easily be extended to work for a multiple feed-line structure, coupling through a layered system with an aperture, or for different feed line types such as slot lines or strip lines. Thus, the research that was done to develop this model has ultimately provided a fundamental theoretical framework for models of vertical coupling between microstrip lines and finite apertures as well as other types of printed planar feed lines such as strip lines and slot lines.

As a part of developing a model to describe coupling between a microstrip line and a finite slot, an analysis of the validity of the Knorr model [5] and the Das model [6] has been performed. These models were tested against HFSS simulation results as well as the model proposed in this thesis by using the coupling impedance metric Z. These models, in general, aligned with the expected HFSS coupling impedance result except for a slight magnitude and frequency shift. The model

proposed in this thesis rivals the accuracy of these previously proposed models. It is also less computationally intensive than the Das model, in general. A closed form expression is provided by Das for the rigid case of coupling between a microstrip line and an slot line extending a quarter wavelength past the transition region. For structures that vary from this physical constraint, the Das model may approach the computational intensity of a full wave solver. Beyond this, the model proposed in this thesis is more robust than the Knorr model because it takes into account both electric and magnetic coupling effects.

In addition, a link between Lorentz Reciprocity Theorem and General Coupling Theory [12] has been derived. The link between these theories lies with the mutually stored energy that was derived and defined in this thesis. The difference between the coupling coefficient provided by General Coupling Theory and the turns ratio of an ideal transformer has also been clarified. It was found that the coupling coefficient and the turns ratio of an ideal transformer are not the same quantities. This is an important clarification as it may be a common point of confusion for some engineers.

Future research on this topic will require the development of a more comprehensive model for the fringing fields at the slot edges beyond the simple electric field perturbation and modified propagation constant method used in the proposed model. Beyond this, the coupling model can be made more rigorous by including higher order modes of the microstrip line in the microstrip field model beyond the TEM approximation used as a part of this research as well as an improved model for the fringing effects along the length of the microstrip line. Further research should also be done to derive the link between the proposed model and the mutually stored energy that has been defined in this thesis.

Bibliography

[1] J. E. Ruyle, *Small, Dual Band, Placement Insensitive Antennas*. PhD thesis, University of Illinois, Illinois, 2011.

[2] J. E. Ruyle, "Electrically small slot antenna design tool," *Presentation, Univ. of Oklahoma*, 2015.

[3] L. Szolc, T. Poydence, and J. Ruyle, "Frequency-agile ring resonator end-loaded slot antenna (elsa)," *Submitted to IEEE Antennas and Wireless Propagation Letters*.

[4] D. M. Pozar, *Microwave engineering; 3rd ed.* Hoboken, NJ: Wiley, 2005.

[5] J. Knorr, "Slot-line transitions," *IEEE Transactions on Microwave Theory and Techniques*, 1974.

[6] N. Das, "Generalized multiport reciprocity analysis of surface- to-surface transitions be tween multiple printed transmission lines," *IEEE Transactions on Microwave Theory and Techniques*, vol. 41, no. 6, 1993.

[7] D. Pozar, "A reciprocity method of analysis for printed slot and slot-coupled microstrip antennas," *IEEE Transactions on Antennas and Propagation*, vol. 34, pp. 1439–1446, Dec 1986.

[8] J. Volakis, M. Nurnberger, and D. Filipovic, "Slot spiral antenna," *IEEE Antennas and Propagation Magazine*, vol. 43, pp. 15–26, Dec 2001.

[9] H. Huang and Z. Lv, "A spiral antenna with integrated parallel-plane feeding structure," *Progress In Electromagnetics Research Letters*, vol. 45, pp. 45–50,

2014.

[10] T. Debogovic, A. Karabelj, and J. Bartolic, "Dual band reconfigurable slot antenna with high frequency ratio," in *2008 Microwaves, Radar and Remote Sensing Symposium*, pp. 22–25, Sept 2008.

[11] "User's guide – high frequency structure simulator, v10," *Ansoft Corporation*, June 2005.

[12] J.-S. Hong, *Microstrip Filters for RF/Microwave Applications, 2nd Edition*. 2011.

[13] M. Himidi, O. Lafond, and J. Daniel, "Cavity method for slot-fed patches: Inclined line, circular polarization," 1999.

[14] L. Liu, Z. Ghassemlooy, A. Sambell, S. Danaher, Q. Lu, and E. Korolkiewicz, "Investigation of transformers' turn ratios and design procedure for an aperture coupled slot antenna," *Active RF Devices, Circuits and Systems Seminar*, pp. 61–65, 2011.

[15] S. Cohn, "Slot line on a dielectric substrate," *IEEE Transactions on Microwave Theory and Techniques*, vol. 17, pp. 768–778, Oct 1969.

[16] E. Brenner and M. Javid, *Analysis of Electric Circuits, Second Edition*. McGraw-Hill, 1967.

[17] D. Cheng, *Field and Wave Electromagnetics, 2nd Edition*. 1989.

[18] E. Hammerstad and O. Jensen, "Accurate models for microstrip computer-aided design," in *Microwave symposium Digest*, pp. 407–409, May 1980.

[19] R. Garg, I. Bahl, and M. Bozzi, *Microstrip lines and slotlines*. Artech house, 2013.

[20] F. Tischer, "Slot compensation in a standing-wave meter at millimeter waves,"

1967.

[21] R. Janaswamy and D. H. Schaubert, "Characteristic impedance of a wide slot-line on low-permittivity substrates (short paper)," *IEEE Transactions on Microwave Theory and Techniques*, vol. 34, pp. 900–902, Aug 1986.

[22] S. Cohn, "Slot-line field components," *IEEE Microwave Theory and Techniques Society*, vol. 20, no. 2, pp. 172–174, 1972.

[23] J. Harlow, *Electric Power Transformer Engineering*. CRC Press, 2004.

[24] "Chapter 11: Inductance and magnetic energy." http://web.mit.edu/8.02t/www/materials/StudyGuide/guide11.pdf, 2013 (accessed December 5th, 2016).